Neural tube organoids self-organise floorplate through BMP-mediated cluster competition

Teresa Krammer*[1], Hannah T. Stuart*[1,2], Elena Gromberg*[1], Keisuke Ishihara[1,3], Manuela Melchionda[2], Jingkui Wang[1], Elena Costantini[1], Stefanie Lehr[4], Dillon Cislo[5], Laura Arbanas[1], Alexandra Hörmann[6], Ralph A. Neumüller[6], Nicola Elvassore[7], Eric Siggia[5], James Briscoe[2], Anna Kicheva[4], Elly M. Tanaka[1#]

[1] Research Institute of Molecular Pathology (IMP), Vienna, Austria
[2] The Francis Crick Institute, London, UK
[3] Current address: University of Pittsburgh, Pittsburgh, USA
[4] Institute of Science and Technology Austria (ISTA), Vienna, Austria
[5] Center for Studies in Physics and Biology, The Rockefeller University, New York, USA
[6] Boehringer Ingelheim RCV GmbH & Co KG, Vienna, Austria
[7] Department of Industrial Engineering, University of Padova & Veneto Institute of Molecular Medicine (VIMM), Padova, Italy
* Co-first authors
# Corresponding author

Abstract

The neural tube (NT) has been a hallmark example of embryonic induction and patterning whereby the notochord induces an organiser, the floorplate, that secretes Sonic Hedgehog (SHH) to pattern the surrounding field of neural progenitors. On the other hand, NT organoids (NTOs) formed from embryonic stem cells (ESCs) undergo spontaneous floorplate formation and patterning in the absence of their normal embryonic inducers. Understanding how stem cells undergo regulative organiser formation is a central challenge in biology. Here, we investigated the self-organisation of a SHH-expressing floorplate organiser using clonal NTOs. Expression of FOXA2, a floorplate transcription factor, was initially spatially scattered before resolving into multiple clusters. These FOXA2^{+} clusters underwent competition and physical sorting, resulting in a stable "winning" floorplate. We identified BMP signalling as a key governor of long-range cluster competition. FOXA2^{+} clusters expressed BMP4 ligand suppressing FOXA2 in receiving cells, while simultaneously expressing the BMP-inhibitor NOGGIN to secure FOXA2^{+} cluster survival. Genetic mutation of *Noggin* perturbed the floorplate not only in NTOs but also *in vivo* at the mid-hindbrain region of the mouse NT. These results demonstrate how the floorplate can form autonomously without its well-known inducer, the notochord, suggesting redundant mechanisms ensuring robustness. Defining molecular pathways that govern organiser self-organisation is critical in harnessing the developmental plasticity of stem cells toward directed tissue engineering.

Introduction

During vertebrate development groups of cells called organisers secrete morphogens to induce cell fate patterning in the surrounding tissues [1,2]. In the embryo, organisers are induced by interaction of emerging tissues (reviewed in [3]). Correct organiser placement relies on pre-existing asymmetries in the embryo and the delivery of polarising cues. Intriguingly, recent discoveries *in vitro* have found that organisers can form by a process of self-organisation, in the absence of their natural developmental inducers [4–7]. Despite their central importance for multicellular development, as well as tissue regeneration and engineering, the mechanisms by which organisers self-organise are poorly understood.

The neural tube (NT) is the embryonic precursor of the central nervous system. Patterning of neural progenitor identities along the body axes ensures the formation of the correct diversity and arrangement of neurons [8,9]. In the developing spinal cord, NT patterning along the dorsal-ventral axis is driven by two opposing organisers: the dorsal roofplate secreting BMPs and WNTs, and the ventral floorplate secreting SHH morphogen [10–13]. *In vivo*, the ventral floorplate organiser is usually induced by SHH and other signals from the underlying notochord [14,15], which has been most extensively studied at thoracic levels. The more anterior floorplate is induced earlier during amniote gastrulation [14,16,17] and forms independently of notochord signalling by a mechanism that is currently unclear.

Remarkably, SHH-expressing floorplate has been shown to self-organise in NT organoids (NTOs) *in vitro* [6] in the absence of notochord or any directional inductive cues. NTOs form clonally, by differentiating single mouse embryonic stem cells (ESCs) embedded in 3D hydrogels [6,18], resulting in neuroepithelial cysts with a single apical lumen that exhibit a "default" dorsal midbrain identity. A global pulse of retinoic acid (RA) applied at Day 2 for 18 hours posteriorises NTOs to hindbrain levels and triggers self-organisation of dorsal-ventral patterning by Day 6 [6] (Figure 1A). This phenomenon is characterised by the formation of a localised $FOXA2^{+}SHH^{+}$ floorplate at the emergent ventral pole, which then drives ventral-to-dorsal patterning of neural progenitor identities. Here, we address the mechanism governing the self-organisation of this floorplate organiser in NTOs.

Results

FOXA2$^+$ floorplate precursors self-organise from a spatially scattered to clustered state in clonal NTOs.

To characterise the spatiotemporal dynamics of how the FOXA2$^+$SHH$^+$ floorplate self-organises in NTOs, we first performed timecourse immunofluorescence (IF) staining after RA pulse (Figure 1A). We assayed FOXA2, SHH and SHH/GLI-responsive NKX6.1 (Figure 1B) and quantified the number of NTOs expressing each marker (Figure 1C). Temporally, FOXA2 expression was observed from Day 3 onwards, in >80% of NTOs, prior to detection of SHH or NKX6.1 proteins. From Day 5-6, the number of NTOs with FOXA2 and detectable SHH/NKX6.1 increased, whereas SHH or NKX6.1 expression were not observed in FOXA2$^-$ NTOs (Figure 1C), indicating that FOXA2 preceded SHH expression and activity. Accordingly, RNA-seq analysis [19] showed upregulation of *FoxA2* transcript earlier than *Shh* or *Nkx6.1* (Figure S1A). IF and RNA-seq both showed an increase in the level of FOXA2 expression over time from Day 3 onwards (Figure 1B, S1A).

In vivo, SHH from the notochord can induce floorplate FOXA2 expression via GLI binding sites found in FOXA2 regulatory elements [15,20]. Although we observed FOXA2 expression prior to SHH in NTOs (Figure 1B-C, S1A), we nonetheless asked whether genetic deletion of SHH would abolish FOXA2 induction and cluster formation. NTOs formed from *Shh*$^{-/-}$ ESCs showed no detectable SHH or NXK6.1 expression at any timepoint (Figure 1D, S1B). However, FOXA2 induction and cluster formation still occurred in *Shh*$^{-/-}$ NTOs (Figure 1D, S1C). Unlike parental wildtype (WT) NTOs, the proportion of *Shh*$^{-/-}$ NTOs exhibiting FOXA2 expression decreased from 80% to 60% over Days 5–6 (Figure S1B), suggesting a role for SHH in FOXA2 maintenance at later timepoints, consistent with phenotypes of prolonged SHH antagonism in NTOs [6] and the SHH-driven regulatory architecture at the *FoxA2* locus [20].

Spatially, NTOs expressed FOXA2 at Day 3 in a scattered salt-and-pepper manner (Figure 1B). Subsequently, the FOXA2 signal became increasingly clustered, until by Day 5-6 FOXA2 was found in discrete domains, inside which SHH expression commenced to yield a functional floorplate reflected by induction of NKX6.1 (Figure 1B-C). Over time, the proportion of NTOs with scattered FOXA2, versus 3+, 2 or 1 clusters per NTO shifted until a

104 majority of NTOs contained a single FOXA2$^+$ cluster (Figure 1E). To quantify the spatial
105 distribution of FOXA2$^+$ nuclei in 3D, we performed von Mises-Fisher analysis in which a
106 concentration parameter *K* is computed based on the sum of directional vectors from the NTO
107 centre. This confirmed that FOXA2 expression became increasingly concentrated over time
108 (Figure 1F). Together, this shows that floorplate self-organisation in RA-treated NTOs is
109 characterised by "salt-and-pepper" FOXA2 induction, followed by clustering of FOXA2$^+$
110 floorplate precursor cells, which occurs prior to and independently of SHH expression.
111
112
113 **Intermediate FOXA2$^+$ clusters interact via competition and sorting during self-**
114 **organisation.**
115
116 We next sought to understand whether and how individual NTOs progress from
117 scattered to multi-cluster to single floorplates. We generated a FOXA2-Venus fusion reporter,
118 together with knock-in of H2A-mCherry into the safe-harbour *Rosa26* locus to constitutively
119 label nuclei (Figure 2A, S2A-C). Using 3D light-sheet live-imaging, we acquired images every
120 15 minutes starting from Day 3 in over 300 live NTOs (Figure 2B). This revealed self-
121 organisation of FOXA2-Venus$^+$ cells from a spatially scattered to a clustered state via
122 progressive formation of and resolution between intermediate clusters (Figure 2C, Movies S1-
123 2), in agreement with fixed sample quantifications (Figure 1E).
124
125 We observed two distinct modes by which intermediate clusters resolved (Figure 2D,
126 Movies S3-6): 1) cluster extinction, whereby FOXA2-Venus expression was lost in some
127 clusters whilst it persisted in others, and 2) physical cell-sorting, whereby FOXA2-Venus$^+$ cells
128 from one cluster coalesced with another cluster. These two behaviours were not mutually
129 exclusive: 20% of NTOs exhibited both sorting and extinction of FOXA2-Venus$^+$ clusters,
130 whilst 35% and 45% exhibited only sorting or only extinction, respectively (Figure 2E). We
131 focussed on cluster extinction as it was observed in the majority of NTOs.
132
133 To understand if cluster extinction occurred autonomously or via communication
134 (competition) between clusters, we categorised live-imaged NTOs according to the number of
135 FOXA2-Venus$^+$ clusters observed at intermediate versus endpoint times. We then tested
136 statistically whether clusters behaved independently of each other. For NTOs with one
137 intermediate cluster, 14 out of 52 extinguished their cluster during self-organisation (Figure

138 2F). By considering the disappearance of a given cluster as a process with this observed
139 probability, we formulated the null hypothesis that, if FOXA2-Venus$^+$ clusters behave
140 independently, the outcome for NTOs with two intermediate clusters can be explained by
141 multiplying the probabilities. We thus calculated the expected outcomes then compared them
142 with experimental observations (Figure 2F). In live-imaged NTOs with two intermediate
143 clusters, the observed outcomes differed significantly from the expected outcomes. A cluster
144 was significantly more likely to be extinguished if another cluster was present (Figure 2F),
145 indicating competitive communication between the clusters that governs final outcome.
146
147
148 **BMP signalling activity anti-correlates with FOXA2 expression during cluster**
149 **interaction.**
150
151 We sought to determine the molecular signals that facilitate cluster communication. To
152 identify candidates, we performed bulk RNA-seq of sorted FOXA2-Venus positive versus
153 negative cells at Day 5, a timepoint during which cluster extinction was occurring (Figure 3A,
154 S3A). Reasoning that secreted signals could explain long-range mutual inhibition between
155 clusters, we focused on the expression of ligands, receptors, transducers and modulators for the
156 major secreted signalling pathways. Using two methods to test enrichment of signalling
157 pathway signatures in FOXA2$^+$ versus FOXA2$^-$ cells (Figure 3B, S3B), signatures of WNT,
158 FGF and BMP signalling were uncovered in FOXA2$^+$ cells. Various WNT and FGF ligands
159 were expressed in FOXA2$^+$ or FOXA2$^-$ populations (Figure 3C). Notably, BMP ligands were
160 almost exclusively expressed in FOXA2$^+$ cells (Figure 3C). Expression of the secreted WNT
161 inhibitors *Dkk1-3* and secreted BMP inhibitors *Noggin* and *Chordin* was enriched in FOXA2$^+$
162 cells, whereas FGF-responsive *Spry4* was enriched in FOXA2$^-$ cells (Figure 3C). We therefore
163 investigated WNT, FGF and BMP pathways in NTOs, by spatial analyses of signalling
164 activities and functional perturbations as described below.
165
166 To functionally test the candidate pathways, we performed pharmacological screens
167 using small molecules and recombinant proteins to activate or inhibit WNT, FGF or BMP
168 signalling from Day 3-5 (Figure S3C). WNT or FGF perturbations led to a slight decrease in
169 the percentage of FOXA2$^+$ NTOs at Day 5, irrespective of whether the pathway was activated
170 or inhibited. However, BMP activation decreased while inhibition increased the percentage of
171 FOXA2$^+$ NTOs, demonstrating that the level of BMP signalling modulates FOXA2 expression.

172 To assess the activities of the WNT, FGF and BMP pathways during cluster self-
173 organisation in NTOs, we assayed for LEF1, pERK or pSMAD1/5/9 respectively by IF (Figure
174 3D). LEF1 and pERK signal decreased whereas pSMAD1/5/9 increased from Day 3-5,
175 suggesting an increase in BMP pathway activity after RA treatment. Interestingly, we observed
176 that pSMAD1/5/9 signal predominated in FOXA2^{-} cells compared to FOXA2^{+} cells (Figure
177 3D, S3D-E). To measure the degree of spatial correlation between FOXA2 expression versus
178 WNT, FGF or BMP signalling activities, we measured signal intensities along a line that
179 bisected cells in NTOs, circling the lumen, then computed the Pearson correlation coefficients
180 between FOXA2 and LEF1, pERK or pSMAD1/5/9 signals respectively (Figure 3E). We did
181 not observe any type of correlation between FOXA2 and LEF1 or pERK signal. In contrast, a
182 negative correlation was found between FOXA2 and pSMAD1/5/9 intensities, consistent with
183 a role of BMP signalling in FOXA2 suppression. Taken together, the BMP pathway exhibited
184 an appropriate activity pattern and perturbation phenotype to be further considered as a
185 candidate signal by which intermediate FOXA2 clusters interact.
186
187
188 **BMP signalling regulates FOXA2 cluster resolution.**
189
190 To functionally investigate the role of BMP signalling during the phase of cluster
191 competition, we perturbed the BMP pathway from Day 4 onwards using pharmacological and
192 genetic approaches (Figure 4A). To quantitatively assess the effect of perturbations on inter-
193 cluster communication, we adapted our protocol to support the growth of larger NTOs (Figure
194 S4A-C) that correspondingly demonstrated a higher frequency of multiple rather than single
195 FOXA2^{+} clusters (Figure S4D) due to a positive correlation between NTO size and endpoint
196 cluster number (Figure S4E).
197
198 BMP4 ligand treatment led to a dose-dependent decrease in the proportion of NTOs
199 with any FOXA2^{+} clusters persisting at Day 6 (Figure 4B-C). Conversely, BMP pathway
200 inhibition by application of recombinant NOGGIN or the small molecule LDN193189 led to a
201 mild increase in the total proportion of NTOs with any FOXA2^{+} clusters (Figure 4B-C, S3E).
202 When broken down into whether each NTO contained 1, 2 or 3+ clusters, BMP inhibition
203 resulted in a significant increase in the proportion of NTOs with 3+ endpoint clusters (Figure
204 4C). This is consistent with a role of endogenous BMP signalling in promoting FOXA2 cluster
205 extinction, which is alleviated by BMP inhibition.

206 We then tested whether endogenously produced NOGGIN plays a role in regulating
207 FOXA2$^+$ clusters in NTOs by generating *Noggin* mutant (*Nog^{mut}*) ESCs with CRISPR-Cas9
208 (Figure S4F), then subjecting them to NTO formation and BMP pathway perturbations (Figure
209 4D-F). A significantly lower proportion of *Nog^{mut}* NTOs contained any endpoint FOXA2$^+$
210 clusters compared to WT NTOs (Figure 4E). BMP4 treatment led to a further and dose-
211 dependent reduction in the proportion of *Nog^{mut}* NTOs with any FOXA2$^+$ clusters (Figure 4E).
212 Furthermore, when we quantified the size of FOXA2$^+$ clusters, *Nog^{mut}* NTOs and BMP-treated
213 WT NTOs both exhibited significantly smaller FOXA2$^+$ clusters than untreated WT NTOs
214 (Figure 4F). Exogenous application of NOGGIN protein to *Nog^{mut}* NTOs rescued the
215 proportion of FOXA2$^+$ NTOs (Figure 4E) and FOXA2$^+$ cluster size (Figure 4F) to WT levels.
216 We confirmed that the FOXA2 clusters in NOGGIN-treated *Nog^{mut}* NTOs represent functional
217 SHH-expressing floorplates at Day 6 by co-staining for SHH and SHH/GLI-responsive
218 NKX6.1 (Figure 4G-H).
219
220 Together, these data demonstrate that BMP signalling activity level regulates FOXA2$^+$
221 cluster outcomes during NTO self-organisation. BMP pathway activation versus inhibition
222 controlled FOXA2$^+$ cluster extinction versus persistence in a dose-dependent manner, as well
223 as modulating FOXA2$^+$ cluster size. Endogenously, BMP4 ligand and BMP-inhibitor
224 NOGGIN were both expressed by FOXA2$^+$ cells (Figure 3C), leading us to query the regulatory
225 interactions between FOXA2, BMP4 and NOGGIN that underpin self-organisation in NTOs.
226 To examine how BMP signalling affects gene expression response in FOXA2$^+$ cells, we
227 perturbed the BMP pathway in NTOs then sorted according to FOXA2-Venus reporter level
228 and performed RNA-seq after 8 hours, in order to capture early transcriptional responses in
229 nascent FOXA2$^+$ cells (Figure 4I, S4G-I). FOXA2$^+$ cells from BMP4-treated NTOs showed a
230 significant increase in *Noggin* expression (Figure 4I), in agreement with BMP-driven *Noggin*
231 induction reported in human 2D gastruloids [21], indicating a feedback loop in which FOXA2$^+$
232 clusters protect themselves from the BMP ligands they themselves produce (Figure 3C).
233
234 In summary, we propose a FOXA2-BMP4-NOGGIN signalling circuitry that underpins
235 cluster competition during NTO self-organisation (Figure 4J). FOXA2 cells express BMP
236 ligands (Figure 3C) that, plausibly through pSMAD1/5/9, suppress FOXA2 in surrounding
237 cells. NOGGIN, also expressed by FOXA2 cells (Figure 3C) and under feedback control by
238 BMP (Figure 4J), promotes the persistence and size of "winner" clusters.
239

240 **NOGGIN regulates floorplate size in the anterior NT *in vivo.***

241

242 Given our observations in NTOs we asked whether deleting *Noggin* might reduce
243 floorplate size *in vivo*. We crossed mice bearing *Noggin* floxed (*Nog*$^{Fl/Fl}$ or *Nog*$^{Fl/+}$) [22] and
244 *Sox2*$^{CreERT2/+}$ [23] alleles (Figure 5A, S5A), tamoxifen-treated at E5.5 to induce *Nog* conditional
245 knockout (cKO) in the epiblast and harvested embryos at E10.5 to evaluate FOXA2 and SHH
246 expression in the NT at different anatomical levels (Figure 5B).

247

248 By quantifying the DAPI^{+} area in cross-sections, we observed that mutant embryos
249 exhibited slightly smaller NTs in the cervical spine region compared to control embryos from
250 the same developmental stage (Figure S5B). To avoid any confounding effect, we measured
251 the areas of FOXA2 and SHH expression (Figure S5C-D) then normalised to respective NT
252 size (Figure 5C). We found a significant decrease in the normalised areas of FOXA2 and SHH
253 expression in *Nog* cKO compared to control embryos specifically in the mid-hindbrain region,
254 in which the floorplate forms prior to notochord development [24]. By contrast, there was no
255 difference in the FOXA2 and SHH domain sizes in the notochord-dependent cervical and
256 thoracic spinal cord. Altogether, our *in vitro* and *in vivo* findings suggest that floorplate
257 establishment in the mid-hindbrain region is regulated via BMP-dependent cell
258 communication.

Discussion

Here, we describe how a floorplate signalling centre self-organises in clonal 3D NTOs. Following a pulse of RA signal, FOXA2$^+$ cells emerge in a salt-and-pepper fashion at Day 3, then undergo a process of cluster formation and resolution to form a localised domain, in which SHH morphogen expression commences from Day 5 (Figures 1-2). During NTO self-organisation, intermediate FOXA2$^+$ clusters do not behave independently, but instead promote each other's extinction (Figure 2) via a BMP-mediated signalling mechanism, whilst NOGGIN protects FOXA2 (Figures 3-4). Furthermore, BMP4 application or *Noggin* mutation decreases FOXA2 domain size, which can be rescued by exogenous NOGGIN (Figure 4). Strikingly, the expression of BMP ligands and inhibitors are both enriched in the FOXA2$^+$ cells, whereas BMP signal transduction indicated by pSMAD1/5/9 is enriched in FOXA2$^-$ cells (Figure 3). This represents a self-organisation mechanism in which spatially scattered FOXA2$^+$ cells express the signalling machinery driving their competition to result in a ventral pole. Future advances will allow us to understand cluster competition in NTOs more deeply, such as how FOXA2 levels or cluster size are controlled and how these properties relate to the ultimate outcome. A thorough understanding will also involve developing the means to determine the localization and dynamics of the BMP pathway components.

Expression of both the FOXA2 "inhibitor" (BMP4) and "activator"/protector (NOGGIN) molecules from the same cells (FOXA2$^+$), and the feedback by which BMP4 promotes *Noggin* expression in FOXA2$^+$ cells (Figure 4), displays features of a reaction-diffusion (RD) mechanism [25,26]. In the future, it will be interesting to test the extent to which an RD-type mechanism underpins floorplate patterning in NTOs. This NTO system also offers the intriguing possibility to define quantitatively how the relative contributions of long-range communication versus physical cell sorting mechanisms (Figure 2) complement each other to promote self-organisational robustness. It will also be interesting to see how our findings from mouse stem cells compare to recently described human NTOs that induce full or partial DV patterning [27–29]. In those studies, fixed timepoint analysis showed scattered FOXA2 prior to floorplate formation, but as less than 30% of human NTOs formed floorplates, it has been unclear whether the scattered starting point was an intermediate to the final state, or whether distinct subpopulations arose over time [27]. WNT signalling has been proposed to act in an RD patterning system in human NTOs [29], which we did not observe in mouse NTOs. Whether these

292 discrepancies are due to experimental approaches or whether they highlight intriguing inter-
293 species differences remains to be addressed.
294
295 Other 3D organoid models that form from aggregates of 100s-1000s of cells [30–34] can
296 self-organise by amplifying initial asymmetries, yielding persistence of a signalling centre at
297 the location of its initial emergence. In contrast, our NTOs form clonally from single ESCs and
298 show a regulative self-organisation process, with nascent clusters competing via long-range
299 signalling prior to establishing a stable ventral organiser. To our knowledge, cluster
300 competition has not been observed in other organoid systems, although few studies have yet
301 interrogated the earliest stages of their self-organisation due to constraints in efficiency,
302 topographic predictability or optical density that have limited tractability. Recent works
303 addressing how 3D gastruloids initiate self-organisation of an anterior-posterior axis [35,36] have
304 combined improvements in homogeneity of input cells and analytical tools to elucidate how
305 early variation in Nodal/BMP and cell position act prior to heterogeneity in WNT activity that
306 determines which cells will form the posterior pole, reinforced by cell sorting. Endogenous and
307 exogenous BMP signalling have been shown to mediate organised lineage induction in 3D
308 models of human epiblast [37,38] and mouse appendages [39], but again without evidence of cluster
309 competition. The processes we describe here are also distinct from those found in clonal
310 intestinal organoids where local activation of YAP1 induces symmetry breaking via DLL1 to
311 determine the future crypt [40], without indication of competition between emergent DLL1 sites.
312 An interesting question is whether mechanisms such as those we describe may be upstream of
313 self-organisation mechanisms in other organoids.
314
315 Here we have identified and tested the importance of BMP signalling for cluster
316 interactions in mouse NTOs. Since BMP is a key morphogen driving dorsal patterning of the
317 NT from the dorsal roofplate organiser [41–43], it seems surprising to observe BMP ligand
318 expression in ventral floorplate cells. However, BMP ligands are reported to be expressed in
319 the *in vivo* floorplate [44–46], in keeping with the enrichment of BMP ligand expression we
320 observe in FOXA2^{+} cells of NTOs (Figure 3). Our observation that BMP4 and NOGGIN
321 regulate floorplate formation and size in NTOs led us to investigate whether BMP signalling
322 circuitry plays a role in floorplate formation *in vivo*. Conditional knockout of *Noggin* in the
323 epiblast led to a reduction in floorplate size at E10.5, particularly at mid/hindbrain regions of
324 the NT where the floorplate, like our NTOs, forms in the absence of underlying notochord

325 (Figure 5). This raises the possibility that ventral sources of BMP may also contribute to NT
326 patterning defects in mouse mutants of the BMP pathway [44–46].
327
328 The broader applicability of the BMP-NOGGIN circuit regulating floorplate formation
329 in NTOs highlights the potential of tractable *in vitro* self-organising systems to uncover
330 mechanisms that may contribute *in vivo*, away from the complexity of the developing embryo.
331 This raises fascinating possibilities for the future: by integrating classical developmental
332 biology with self-organisation in stem cell models, we can quantitatively tease apart how
333 embryonic context and inductive cues interface with self-organising modules, to allow
334 regulative yet robust outcomes of vertebrate development.

335 **FIGURE 1**

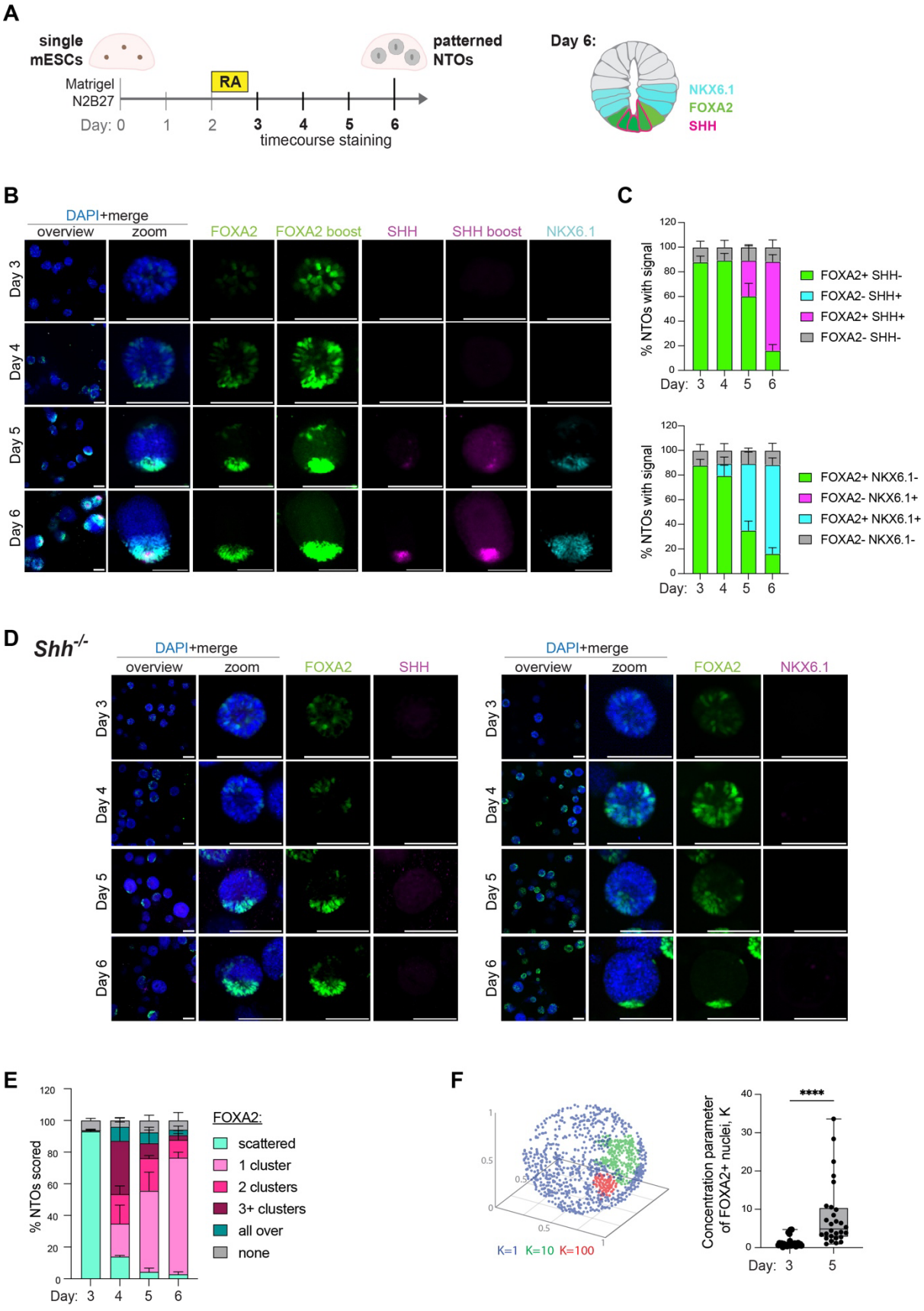

336

Figure 1: Clonal NTOs transition from a scattered expression of FOXA2$^+$ cells to a clustered state which can occur in the absence of SHH.

A: Schematic of NTOs formation. Single embryonic stem cells form epithelial NTOs within two days in Matrigel and N2B27. An 18-hour pulse of retinoic acid induces floorplate formation and DV patterning at the endpoint Day 6.

B: IF timecourse of NTOs fixed from Day 3-6 showing (from left to right, single *z* slice) a merged overview image at 10x magnification, and a representative NTO (zoom) stained for DAPI (blue) and the DV patterning markers FOXA2 (green), SHH (magenta), NKX6.1 (cyan). In the second FOXA2 column, FOXA2 images were scaled with lower maximal grayscale value to highlight the early spatial pattern. In the second SHH column, the same metric was applied. Scale bars, 100 µm.

C: Quantification of marker expression in (n = 528) NTOs over time. Coloured bars correspond to staining in B (n = 192 for Day 3, n = 158 for Day 4, n = 134 for Day 5 and n = 44 for Day 6).

D: *Shh*$^{-/-}$ NTOs undergo FOXA2-cell clustering. Timecourse of *Shh*$^{-/-}$ NTOs fixed from Day 3-6 showing (from left to right, single *z* slice) a merged overview image at 10x magnification, and a representative NTO (zoom) in stained for DAPI (blue) and the DV patterning markers FOXA2 (green) and SHH or NKX6.1 (magenta). For parental control, see Figure S1. Scale bars, 100 µm.

E: FOXA2$^+$ cell cluster distribution over time. FOXA2 spatial distribution was classified into "scattered", "1 cluster", "2 clusters", "3 or more clusters", "none" (FOXA2$^-$), or "all over" (almost entirely FOXA2$^+$). A total of 1148 NTOs were manually analysed (n = 292 for Day 3, n = 285 for Day 4, n = 209 for Day 5 and n = 362 for Day 6).

F: FOXA2$^+$ cell clustering analysis using von Mises–Fisher parameter. Left: Schematic illustrating quantitative clustering parameter (K, from von Mises–Fisher). Right: von Mises–Fisher analysis of 3D FOXA2$^+$ cell distribution in Day 3 (n = 27) and Day 5 (n = 28) NTOs. By Day 5, FOXA2-expressing cells show a higher K value. Each dot represents the K value of a single NTO. Results were statistically analysed using Mann-Whitney test with p = <0.0001. Error bars show standard deviation (SD), asterisks mark statistical significance.

366 **FIGURE 2**

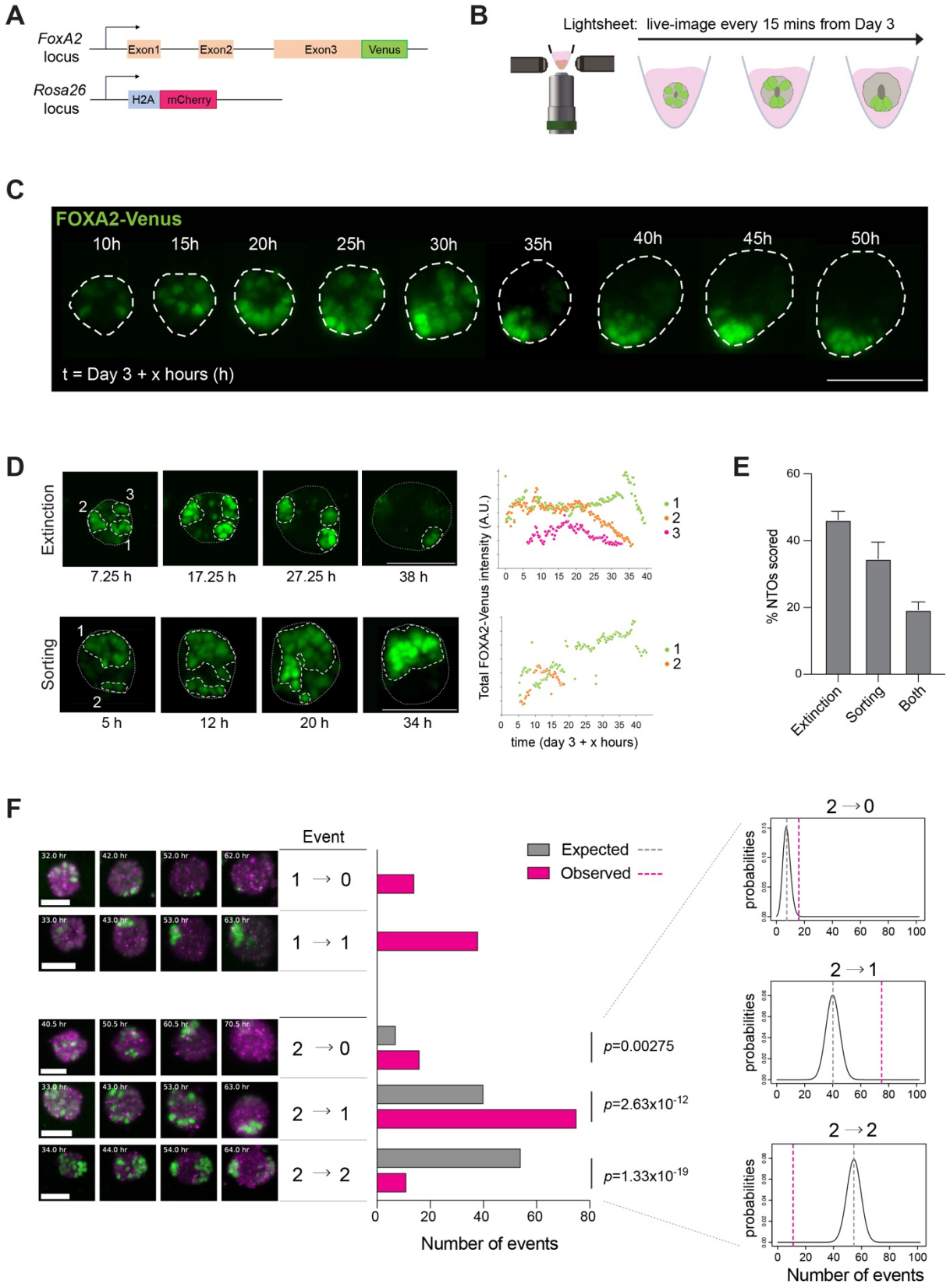

367

368 **Figure 2: Statistical analysis of live cluster dynamics reveals cluster competition during**
369 **self-organisation.**
370 **A:** Schematic of double reporter generation. Venus was knocked in after the 3rd exon at the C-
371 terminus of the endogenous FOXA2 locus generating a fusion protein. In addition, an H2A-
372 mCherry construct was knocked into the ubiquitously expressed Rosa26 locus to mark nuclei.
373 **B:** Schematic (created with BioRender) of timelapse imaging of double reporter on the Viventis
374 lightsheet microscope. Full image stacks with 3 µm *z* step size were taken every 15 mins
375 starting 6 hours post RA removal on Day 3 for 48-75 hours.
376 **C:** Images from timelapse series of a NTO (maximum intensity *z*-projections) following the
377 spatial organisation of FOXA2 (green) over 50 hours showing self-organisation from a
378 dispersed (salt-and-pepper) into a clustered state (see Movies S1-2). Dashed white lines mark
379 the outlines of the NTO. Scale bar, 100 µm.
380 **D:** Two distinct modes of cluster formation. Selected maximum intensity *z*-projection images
381 from two (upper and lower) NTO timelapse series. Upper: "Extinction": three $FOXA2^+$ (green)
382 clusters form, and then one remains while two disappear (see Movies S3-4). Lower: "Sorting":
383 Two distinct clusters grow and coalesce into a single cluster over time (see Movies S5-6).
384 Right: Cluster intensities were tracked over time in graphs. Dotted grey lines mark the outlines
385 of NTOs, dashed white lines mark the outline of $FOXA2^+$ clusters. Scale bars, 100 µm.
386 **E:** A total of $n = 93$ NTOs from three different timelapses that displayed as 2→1 behaviour
387 were subclassified into their mode of self-organisation (extinction, sorting, or both), taking into
388 account that sorting might be overestimated due to analysis using maximum intensity *z*-
389 projections.
390 **F:** Left: representative timecourse images for each category shown as maximum intensity *z*-
391 projections, scale bars 50 µm, and scoring of NTOs according to FOXA2-$Venus^+$ cluster
392 numbers at intermediate vs endpoint times. Middle: based on the frequency of cluster
393 disappearance in NTOs with one intermediate cluster ($n = 52$), the expected outcomes (grey)
394 for NTOs with 2 intermediate clusters ($n = 102$) were calculated using binomial distribution
395 assuming independent cluster behaviour, then compared to observed outcomes (magenta).
396 Right: calculation of p values based on the binomial distribution for each case, with the
397 expected value indicated by grey lines and the observed numbers by magenta lines.

398 **FIGURE 3**

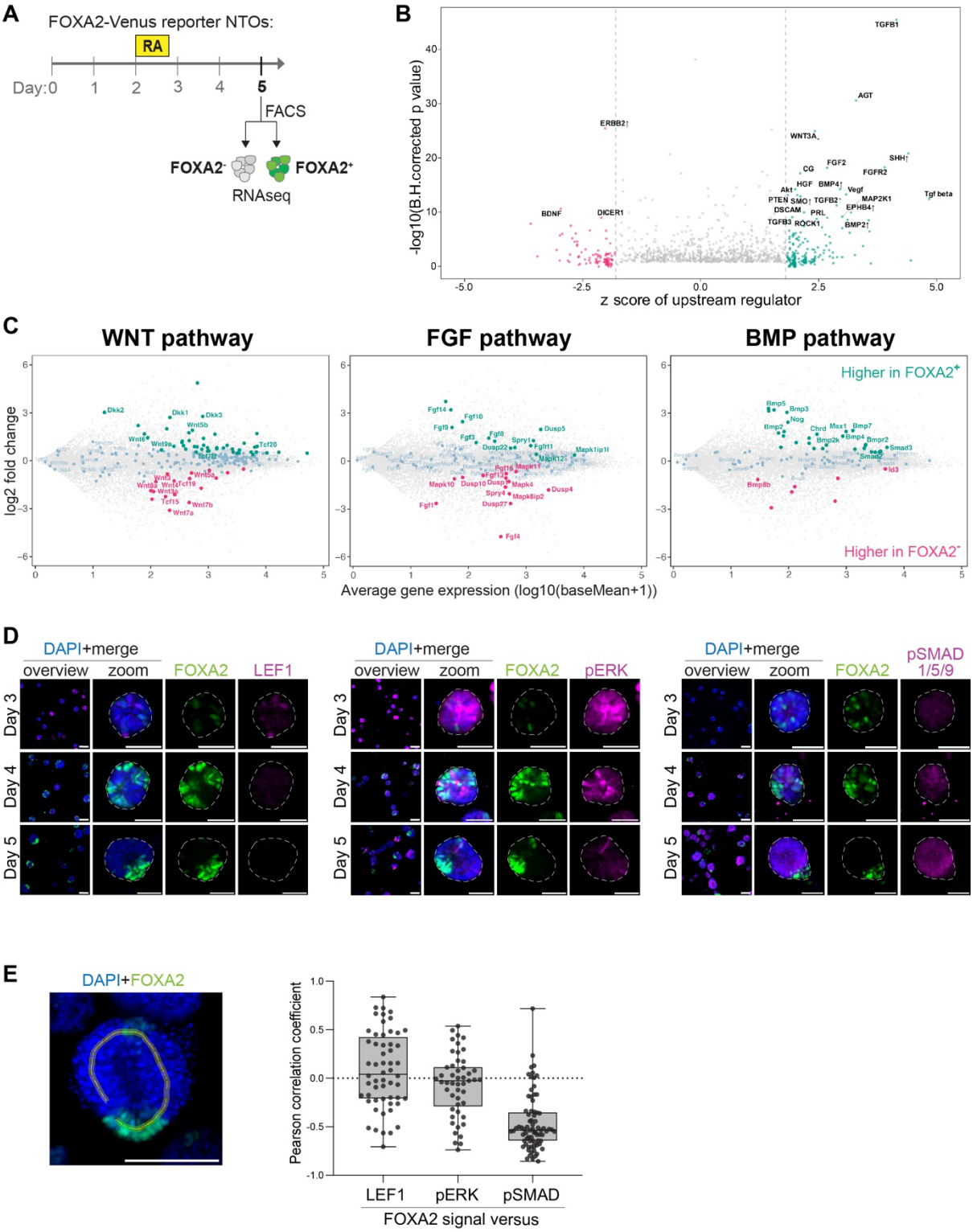

399

400 **Figure 3: FOXA2$^+$ cells express *BMP*s and *Noggin* while FOXA2$^-$ cells display higher**
401 **pSMAD 1/5/9 signal.**
402 **A:** Schematic of RNA-seq performed on sorted FOXA2$^+$ and FOXA2$^-$ cell populations of Day
403 5 NTOs made from the reporter cell line.
404 **B:** Activity plot of upstream regulators predicted to be activated or inhibited based on the
405 observed expression changes in FOXA2$^+$ versus FOXA2$^-$ cells. Regulators are coloured based
406 on activation Z-score at a threshold of 1.8, and the top 20 candidates based on significance are
407 labelled; an arrow next to a regulator name indicates significant up or down regulation of the
408 gene in FOXA2$^+$ (vs FOXA2$^-$).
409 **C:** WNT, FGF and BMP pathway members showing differential gene expression between
410 FOXA2$^+$ and FOXA2$^-$ cells. MA-plot of the RNA-seq data showing log2 fold changes of
411 genes over their average gene expression against samples (*y* axis: FOXA2$^+$ versus FOXA2$^-$ log
412 ratio values, *x* axis: log10(baseMean+1) of average gene expression). Colour highlights genes
413 assigned to either WNT signalling pathway (GO:0016055), FGF signalling pathway
414 (GO:0008543), or BMP signalling pathway (GO:0030509) based on Ensembl 94 annotation.
415 Data point colour indicates up-regulated in FOXA2$^+$ (green, #009988), up-regulated in
416 FOXA2$^-$ (pink, #EE3377) or not significantly differentially regulated genes (light blue).
417 **D:** Time course of NTOs fixed from Day 3-5 (single *z* slice) showing a merged image at 10x
418 magnification, and a representative NTO (zoom) stained for DAPI (blue), FOXA2 (green) and
419 LEF1 to visualise WNT (left)/ pERK to visualise FGF (middle)/ pSMAD1/5/9 to visualise
420 BMP pathway activity (right) (magenta). Dashed white lines mark the outlines of the NTOs.
421 Scale bars, 100 µm for 10x, and 50 µm for zoom of representative NTOs.
422 **E:** Analysis of Pearson correlation coefficient. Left: Representative NTO used for the anti-
423 correlation analysis performed on single *z* slices of images on Day 5. For each NTO cross-
424 section, a line with width of 10 pixels (shown in yellow) was drawn around the NTO starting
425 in the FOXA2$^+$ cluster sparing the lumen. Scale bar, 100 µm. Right: Intensity profiles of
426 FOXA2 and LEF1/ pERK/ pSMAD were measured and analysed by calculating the Pearson
427 correlation coefficient by sampling the pixels for two channels (FOXA2 – LEF1, FOXA2 –
428 pERK, FOXA2 – pSMAD). NTOs are n = 56 LEF1, n = 49 pERK, n = 76 pSMAD.

429 **FIGURE 4**

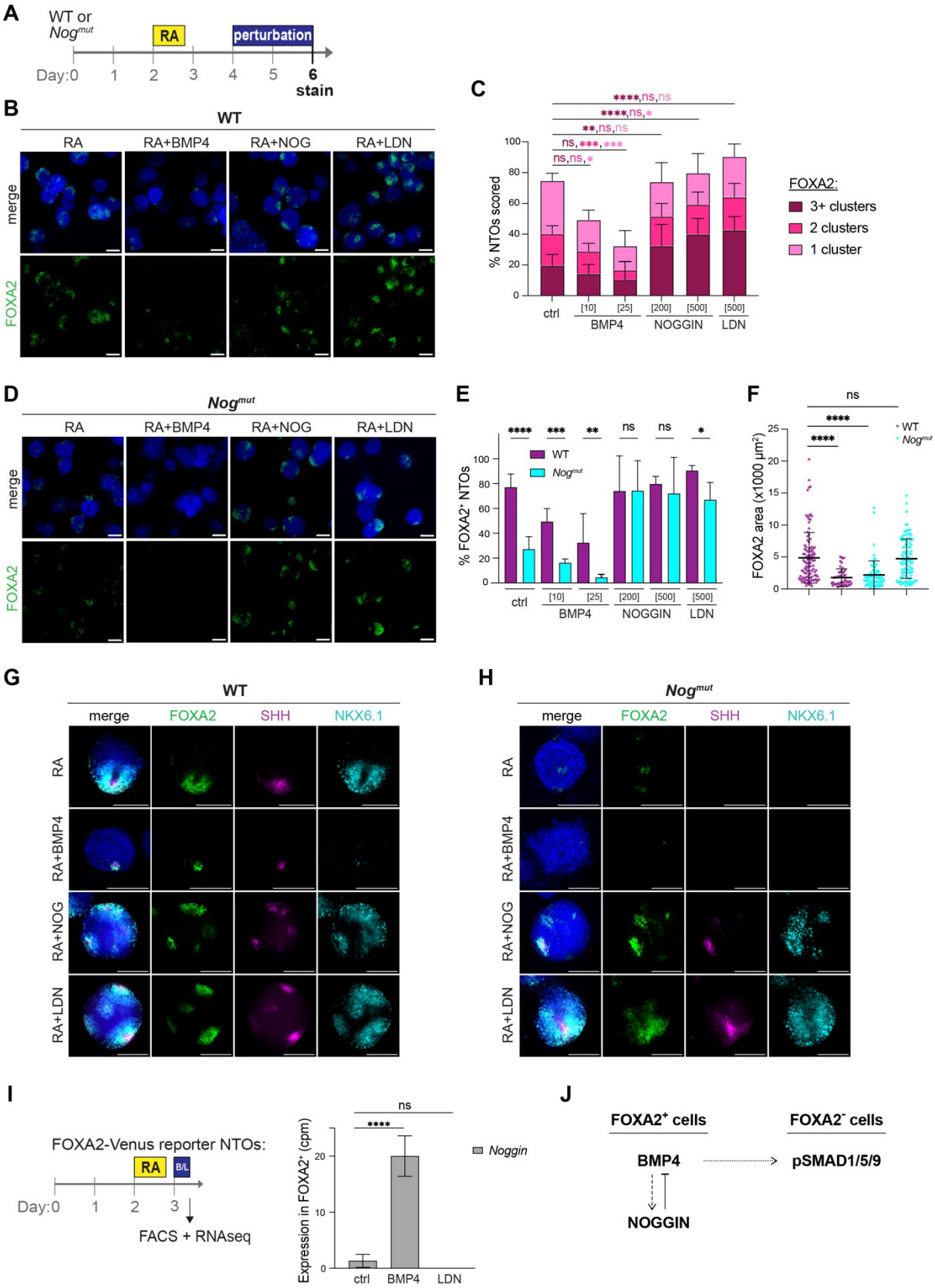

430

431 **Figure 4: BMP pathway activation or suppression modulates FOXA2 cluster persistence.**
432 **A:** Timeline of BMP pathway perturbations using "large NTO" protocol relevant for panels B-
433 H (see Figure S4). Perturbations were performed from Day 4-6 after an 18-hour RA pulse from
434 Day 2-3.
435 **B:** Representative images at 10x magnification (single *z* slice) of WT NTOs stained for DAPI
436 (blue) and FOXA2 (green) for RA, RA+BMP4 (25 ng/ml), RA+NOG (200 ng/ml) and
437 RA+LDN (500 nM). Scale bars, 100 µm.
438 **C:** 3D analysis of numbers of FOXA2$^+$ clusters in WT NTOs on Day 6 shown in B. Results
439 were statistically analysed using an ordinary one-way ANOVA and Dunnettes's multiple
440 comparisons test. For 3 or more clusters: RA vs. RA+BMP4 (10 ng/ml) was n.s., RA vs.
441 RA+BMP4 (25 ng/ml) was n.s, RA vs. RA+NOG (200 ng/ml) p = 0.0029, RA vs. RA+NOG
442 (500 ng/ml) p = <0.0001, RA vs. RA+LDN (500 nM) p = <0.0001; for 2 clusters: RA vs.
443 RA+BMP4 (10 ng/ml) was n.s., RA vs. RA+BMP4 (25 ng/ml) p = 0.0005, RA vs. RA+NOG
444 (200 ng/ml) was n.s., RA vs. RA+NOG (500 ng/ml) was n.s., RA vs. RA+LDN (500 nM) was
445 n.s.; for 1 cluster: RA vs. RA+BMP4 (10 ng/ml) p = 0.0171, RA vs. RA+BMP4 (25 ng/ml) p
446 = 0.0007, RA vs. RA+NOG (200 ng/ml) was n.s., RA vs. RA+NOG (500 ng/ml) p = 0.0153,
447 RA vs. RA+LDN (500 nM) was n.s. Concentration [x] expressed in ng/ml for BMP4 and
448 NOGGIN, or in nM for LDN. Asterisks indicate statistical significance, n.s. indicates non-
449 significance.
450 **D:** Representative images at 10x magnification (single *z* slice) of *Nog^{mut}* NTOs stained for
451 DAPI (blue) and FOXA2 (green) upon RA, RA+BMP4 (25 ng/ml), RA+NOG (200 ng/ml) and
452 RA+LDN (500 nM). Scale bars, 100 µm.
453 **E:** 3D analysis of proportion of FOXA2$^+$ NTOs shown in B and D of WT (purple) and *Nog^{mut}*
454 (cyan). Results were statistically analysed using an ordinary one-way ANOVA, always
455 comparing WT with *Nog^{mut}* samples. RA vs RA p = <0.0001, RA+BMP4 (10 ng/ml) vs
456 RA+BMP4 (10 ng/ml) p = 0.0004, RA+BMP4 (25 ng/ml) vs RA+BMP4 (25 ng/ml) p = 0.0039,
457 RA+LDN (500 nM) vs RA+LDN (500 nM) p = 0.0229, while the other conditions were n.s. A
458 total of n = 3407 (between 306 and 414 per condition) WT NTOs and n = 3425 (between 328
459 and 415 per condition) *Nog^{mut}* NTOs were included in the analysis. Concentration [x] expressed
460 in ng/ml for BMP4 and NOGGIN, or in nM for LDN. Asterisks indicate statistical significance,
461 n.s. indicates non-significance.
462 **F:** 3D analysis of average surface area of FOXA2$^+$ clusters in WT (purple) and *Nog^{mut}* (cyan)
463 NTOs. Each dot represents an average cluster area in a given NTO. Results were statistically
464 analysed using Kruskal-Wallis test and Dunn's multiple comparisons test comparing RA with

465 RA+BMP4 (in WT NTOs), RA and RA+NOG (in *Nog*^{mut} NTOs). WT RA vs WT RA+BMP4
466 p = <0.0001, WT RA vs *Nog*^{mut} RA p = <0.0001, and WT RA vs *Nog*^{mut} RA+NOG was n.s.
467 Asterisks indicate statistical significance, n.s. indicates non-significance.
468 **G:** Representative images (single *z* slice) of a Day 6 WT NTO stained for DAPI (blue), FOXA2
469 (green), SHH (magenta) and NKX6.1 (cyan) for RA, RA+BMP4 (25 ng/ml), RA+NOG (200
470 ng/ml) and RA+LDN (500 nM). Scale bars, 100 µm.
471 **H:** Representative images (single *z* slice) of a Day 6 *Nog*^{mut} NTO stained for DAPI (blue),
472 FOXA2 (green), SHH (magenta) and NKX6.1 (cyan) for RA, RA+BMP4 (25 ng/ml),
473 RA+NOG (200 ng/ml) and RA+LDN (500 nM). Scale bars, 100 µm.
474 **I:** Transcriptional response in FOXA2^{+} cells after BMP signal activation or suppression shows
475 FOXA2^{+} cells induce *Noggin* expression after BMP exposure. Schematic: at Day 3, BMP
476 perturbations were added for 8 hours before NTOs were dissociated and FACS sorted into
477 FOXA2^{+} and FOXA2^{-} cells for RNA analysis. Expression levels (cpm) of *Noggin* in FOXA2^{+}
478 cells upon RA, RA+BMP4 (1.5 ng/ml) and RA+LDN (100 nM) treatments. Results were
479 statistically analysed using DESeq2 with pairwise comparison, RA+BMP4 vs RA p = <0.0001
480 for *Noggin* expression. Asterisks indicate statistical significance, n.s. indicates non-
481 significance.
482 **J:** Model of conceptional interactions between BMP4 and NOGGIN activities in FOXA2^{+} cells
483 and their interaction via pSMAD 1/5/9 activity in FOXA2^{-} cells.

484 **FIGURE 5**

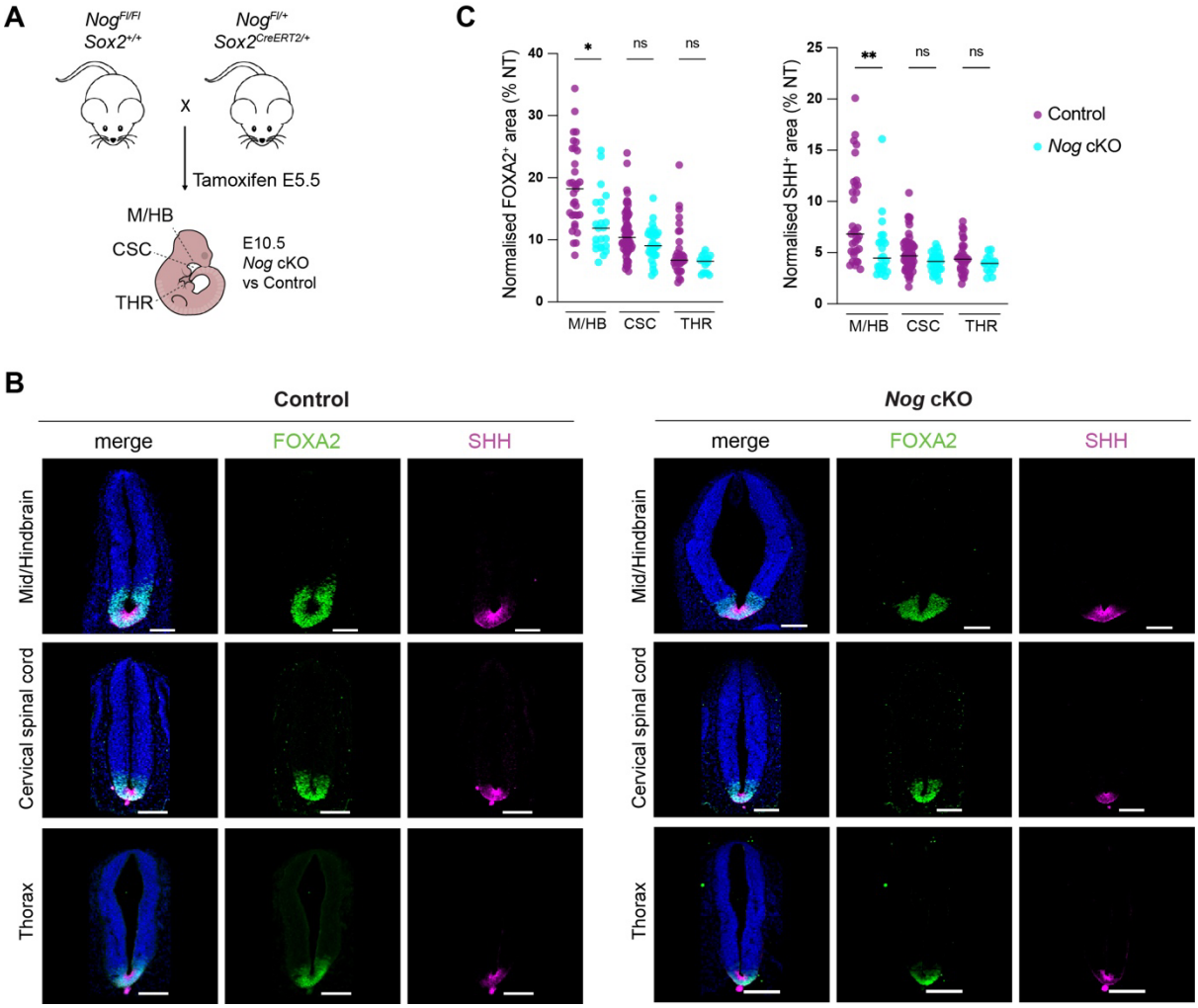

485

Figure 5: *In vivo* role of NOGGIN in anterior floorplate size in the mouse embryo.

A: Schematic of mouse crossing performed for inducible deletion of *Noggin*. E10.5 mouse showing the anatomy and section planes of the harvested and analysed embryos.

B: Representative images of E10.5 Control ($Nog^{Fl/+};Sox2^{+/+}$ or $Nog^{Fl/Fl};Sox2^{+/+}$) and *Nog* cKO ($Nog^{Fl/Fl};Sox2^{CreERT2/+}$) embryos of Mid/-Hindbrain (M/HB), Cervical spinal cord (CSC) and Thorax (THR) regions stained for DAPI (blue), FOXA2 (green) and SHH (magenta). Scale bars, 100µm.

C: Normalised area of FOXA2 and SHH at different anterior-posterior levels of the embryonic NT. Quantification was made on serial sections of 6 Control embryos (N = 136 sections total, 33 for M/HB, 62 for CSC, 33 for THR) in purple and 3 *Nog* cKO embryos (N = 68 sections total, 23 for M/HB, 30 for CSC, 15 for THR) in cyan from two litters. Kruskal-Wallis test and Dunn's multiple comparison tests were performed between anatomical regions of Control vs *Nog* cKO (FOXA2: M/HB vs. M/HB $p = 0.0165$, CSC vs. CSC $p = 0.2706$, THR vs. THR $p = 0.3926$, SHH: M/HB vs. M/HB $p = 0.0031$, CSC vs. CSC $p = 0.0792$, THR vs. THR $p = 0.4484$). Horizontal bars represent means of the data, asterisks indicate statistical significance, n.s. indicates non-significance.

502 **EXTENDED FIGURE S1**

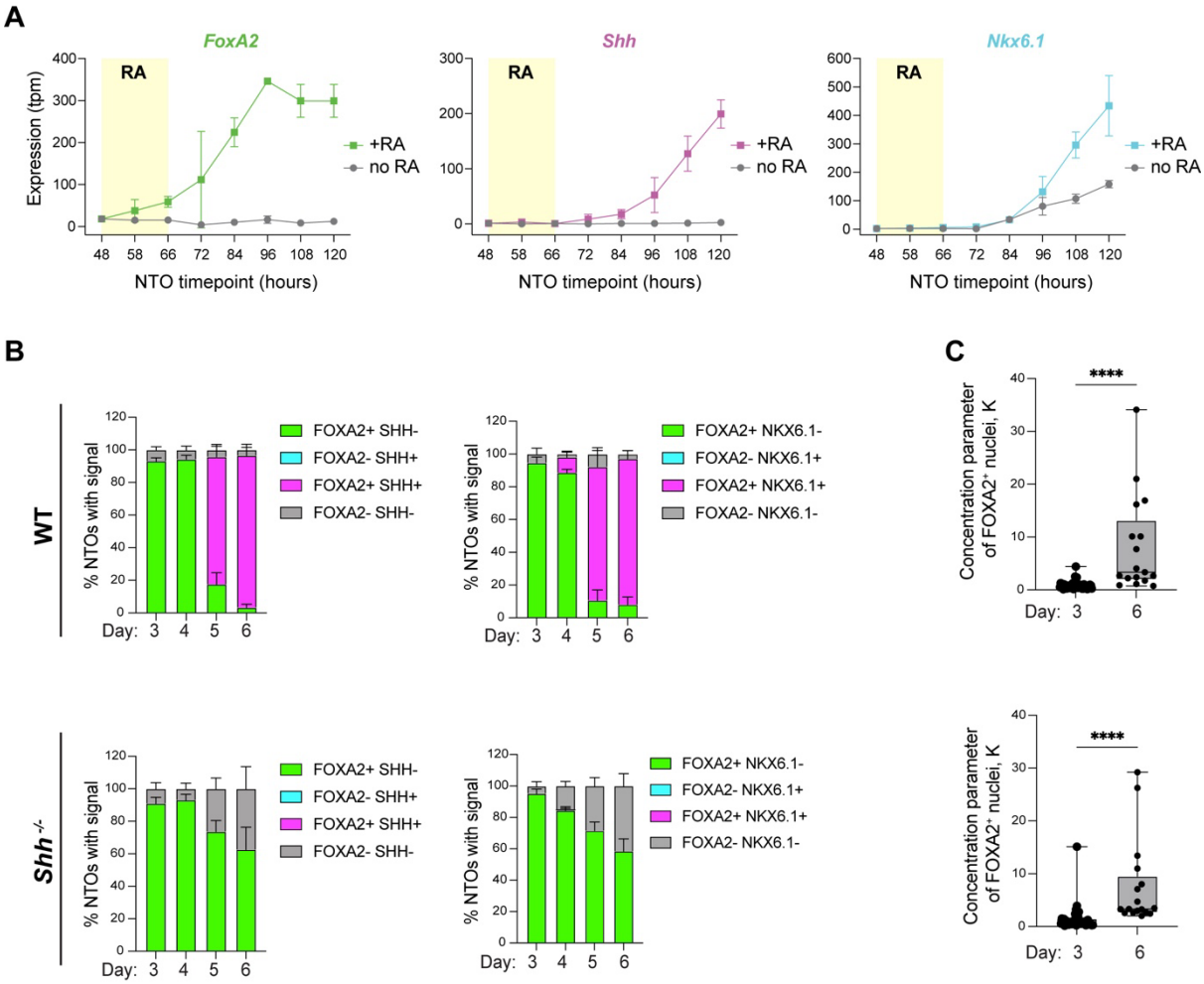

503

504

505 **Extended Figure S1: Characterisation of WT and *Shh*$^{-/-}$ NTO progression.**

506 **A:** Bulk RNA-seq of NTO timecourse shows expression levels of FOXA2, SHH and NKX6.1
507 matching the colours of Figure 1B in transcripts per million (tpm) [19].

508 **B:** 3D quantification of marker expression in *Shh*$^{-/-}$ and parental WT NTOs over time with
509 colours corresponding to *Shh*$^{-/-}$ staining in Figure 1D. n = 2011 NTOs for *Shh*$^{-/-}$ and n = 2239
510 NTOs for WT were used in the analysis of FOXA2/SHH, n = 1142 NTOs for *Shh*$^{-/-}$ and n =
511 1235 NTOs for WT were used in the analysis of FOXA2/NKX6.1.

512 **C:** Concentration parameter, K, measurements of *Shh*$^{-/-}$ NTOs and the corresponding parental
513 WT cell line. Each dot represents the K value of a single NTO (WT: n = 42 for Day 3, n = 17
514 for Day 6, *Shh*$^{-/-}$: n = 41 for Day 3, n = 17 for Day 6). Results were statistically analysed using
515 a Mann-Whitney test with p = <0.0001. Asterisks indicate statistical significance.

516 **EXTENDED FIGURE S2**

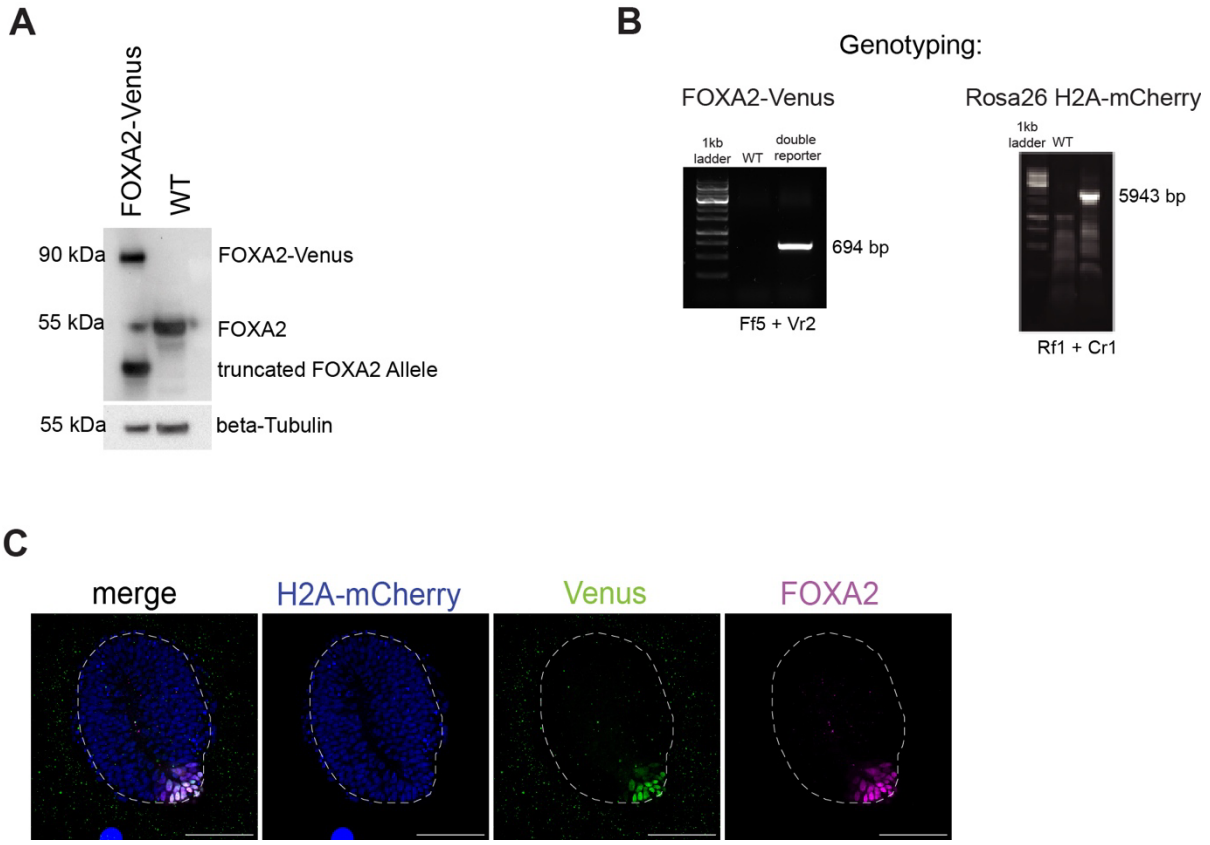

517

518

519 **Extended Figure S2: Characterisation of FoxA2-Venus knock-in line.**

520 **A:** Western Blot of FOXA2-Venus reporter line and WT detecting FOXA2 WT protein,
521 FOXA2-Venus and a truncated FOXA2 allele. Beta-Tubulin served as a loading control.

522 **B:** PCR confirmation of FOXA2-Venus and Rosa26 H2A-mCherry knock in. For Venus
523 insertion, FoxA2_fwd5 (Ff5) and Venus_rev2 (Vr2) (product size: 694 bp), and for mCherry
524 insertion, R26_leftout_fwd1 (Rf1) and mCherry_rev1 (Cr1) (product size: 5943 bp) were used.

525 **C:** Representative Day 5 NTO (single *z* slice) showing co-expression of FOXA2-Venus and
526 endogenous FOXA2 signal with H2A-mCherry (blue), Venus (green) and stained FOXA2
527 (magenta). Dashed lines mark the outlines of the NTO. Scale bars, 100 µm.

528 **EXTENDED FIGURE S3**

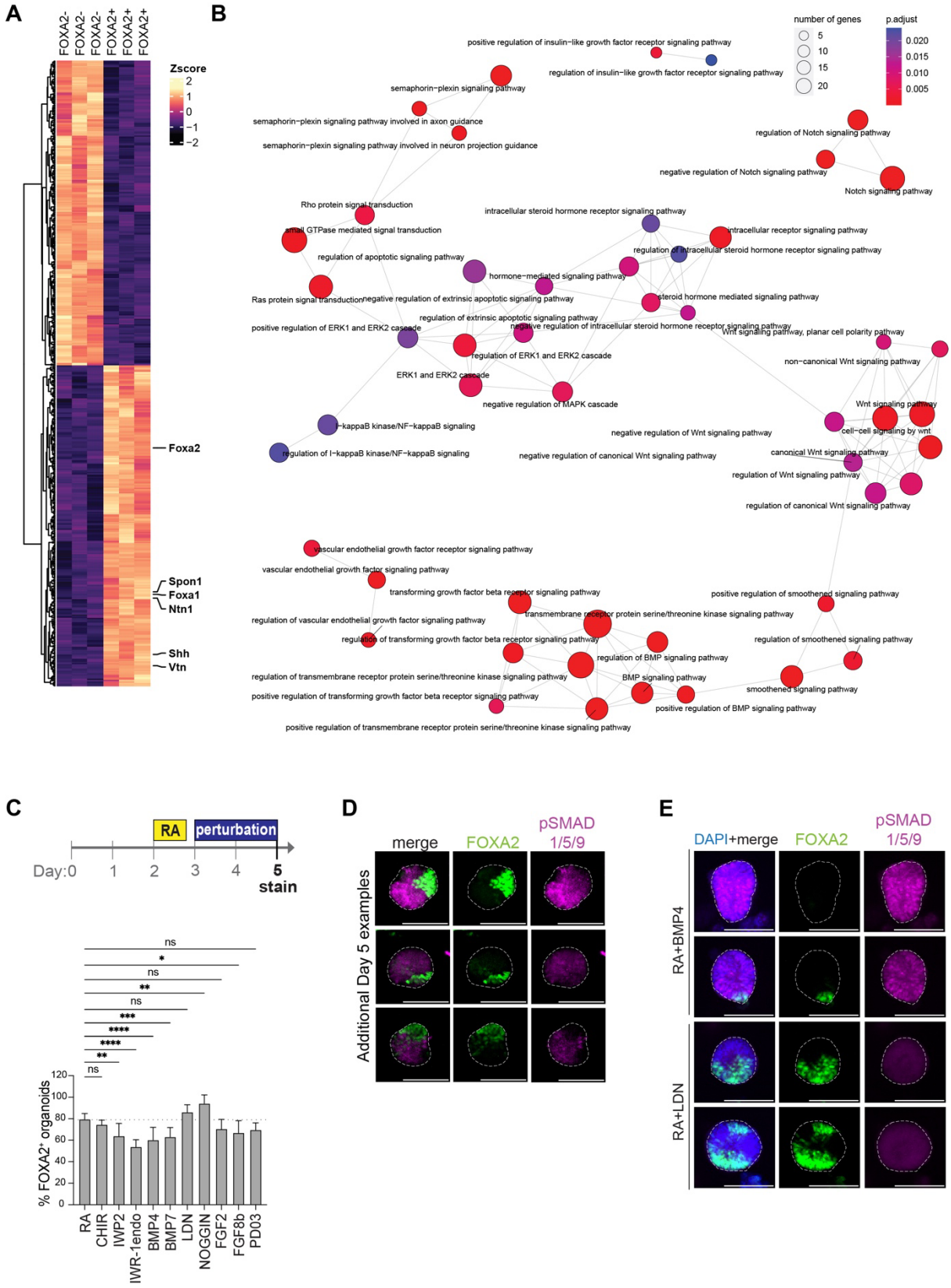

529

530 **Extended Figure S3: Analysis of RNA-seq data from FOXA2$^+$ and FOXA2$^-$ cells and BMP**
531 **analysis.**
532 **A:** Heatmap of clustering of top 500 differentially expressed genes from sorted Day 5 cells.
533 **B:** Enrichment plots showing top 400 genes of various pathways from sorted Day 5 RNA-seq.
534 **C:** Schematic of drug screen performed on Day 3-5 starting on Day 3, i.e. 6 hours post RA
535 removal, with analysis of proportions of FOXA2$^+$ NTOs on Day 5. The following
536 concentrations were used: CHIR (3 µM), IWP2 (5 µM), IWR-1endo (1 µM), BMP4 (5 ng/ml),
537 BMP7 (10 ng/ml), LDN (100 nM), NOGGIN (200 ng/ml), FGF2 (10 µg/ml), FGF8b (200
538 ng/ml), PD03 (1 µM). Results were statistically analysed using an ordinary one-way ANOVA
539 and Dunnettes's multiple comparisons test. RA vs RA+IWP2 p = 0.0019, RA vs RA+IWR-
540 1endo p = <0.0001, RA vs RA+BMP4 p = <0.0001, RA vs RA+BMP7 p = 0.0009, RA vs
541 RA+NOGGIN p = 0.0040, RA vs RA+FGF8b p = 0.0188, while all other tested conditions
542 were n.s. Asterisks indicate statistical significance, n.s. indicates non-significance.
543 **D:** Representative examples (single *z* slice) of Day 5 NTOs stained for FOXA2 (green) and
544 pSMAD1/5/9 (magenta). Dashed lines mark the outlines of the NTOs. Scale bars, 50 µm.
545 **E:** Representative examples (single *z* slice) of Day 5 NTOs stained for DAPI (blue), FOXA2
546 (green) pSMAD1/5/9 to visualise BMP pathway activity (right) (magenta) upon RA+BMP4
547 (1.5 ng/ml), and RA+LDN (100 nM). Dashed lines mark the outlines of the NTOs. Scale bars,
548 100 µm.

549 **EXTENDED FIGURE S4**

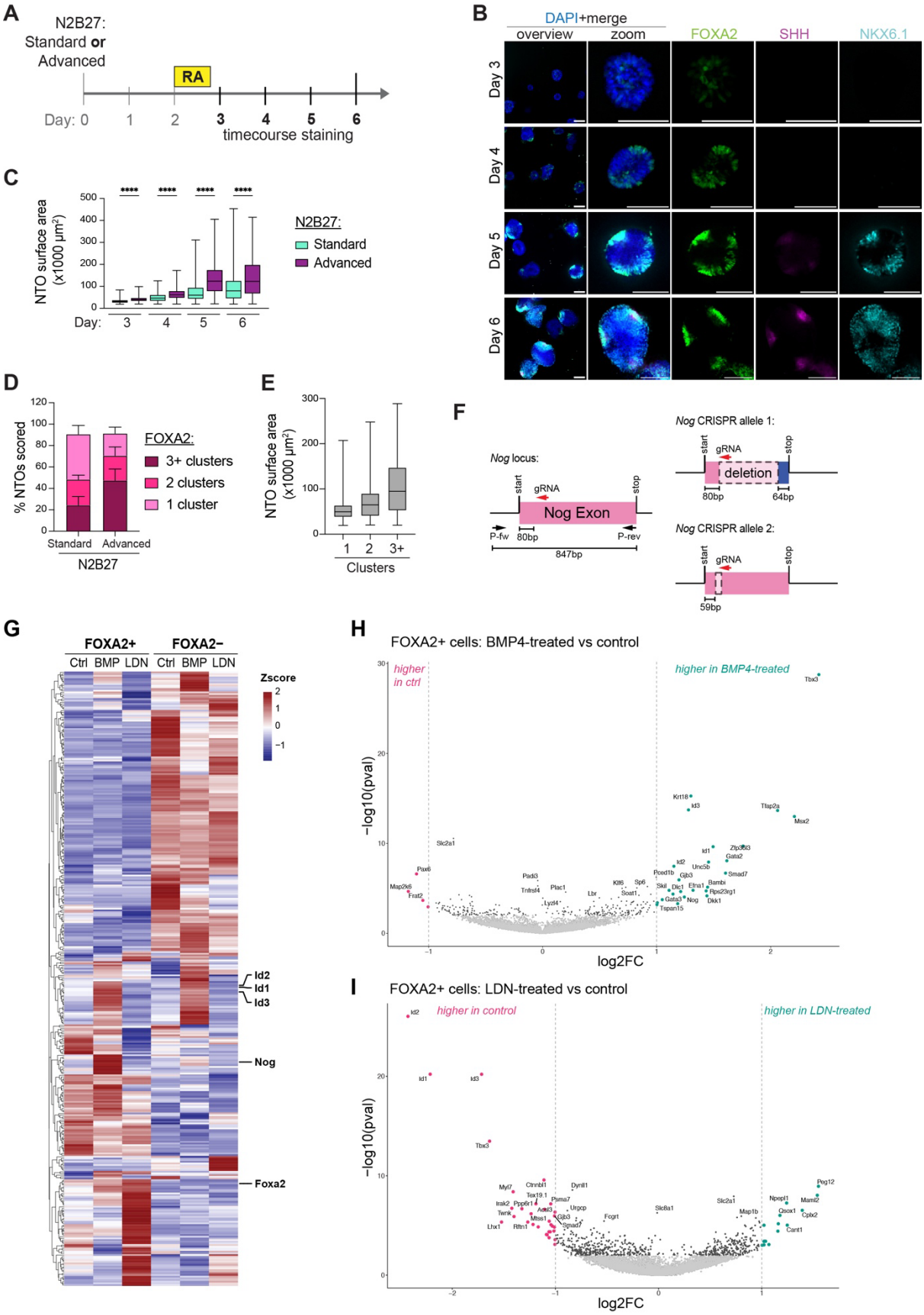

550

551 **Extended Figure S4: Characterisation of large NTOs and transcriptional induction data.**
552 **A:** Basic timeline of NTO production.
553 **B:** IF timecourse of NTOs in rich medium ("Advanced") fixed from Day 3-6 showing (from
554 left to right, single *z* slice) a merged overview image at 10x magnification, and a representative
555 NTO (zoom) stained for DAPI (blue) and the DV patterning markers FOXA2 (green), SHH
556 (magenta), NKX6.1 (cyan). Scale bars, 100 µm.
557 **C:** 3D analysis of NTO surface area in normal NTOs (standard medium, cyan, n = 2463) and
558 large NTOs (advanced medium, purple, n = 1880) from data in Figure 1B and Figure S4B.
559 Asterisks indicate statistical significance.
560 **D:** 3D analysis of numbers of FOXA2$^+$ clusters in WT NTOs on Day 6 from data in Figure 1B
561 and Figure S4B (n = 751 Standard, n = 384 Advanced).
562 **E:** 3D analysis of NTO surface area with 1, 2 or 3+ FOXA2$^+$ clusters (advanced medium, total
563 n = 1321 NTOs, n = 664 for 1 cluster, n = 284 for 2 clusters, n = 373 for 3+ clusters).
564 **F:** Schematic of *Nog^{mut}* cell line generation. The gRNA binds 80bp downstream of the start
565 codon. Sequencing of the mutant clone confirmed a trans-heterozygous mutation. CRISPR
566 allele 1: large deletion followed by a frameshift and premature stop codon, such that only 27
567 amino acids of NOGGIN protein remain, which correspond only to the signal peptide, followed
568 by 21 out-of-frame amino acids. CRISPR allele 2: 33bp deletion including 8 amino acids of
569 the signal peptide and 3 amino acids of NOGGIN.
570 **G:** Heatmap showing clustering of top 200 differentially expressed genes from RNA
571 sequencing.
572 **H:** Volcano plot of genes showing Log2 fold change of expression in RA+BMP4 vs RA in
573 FOXA2$^+$ cells from RNA sequencing. Dark grey: p<0.01, Green (#009988): p<0.01 and FC>2,
574 Pink (#EE3377): p<0.01 and FC<-2.
575 **I:** Volcano plot of genes showing Log2 fold change of expression in RA+LDN vs RA in
576 FOXA2$^+$ cells from RNA sequencing. Dark grey: p<0.01, Green (#009988): p <0.01 and FC>2,
577 Pink (#EE3377): p<0.01 and FC<-2.

578 **EXTENDED FIGURE S5**

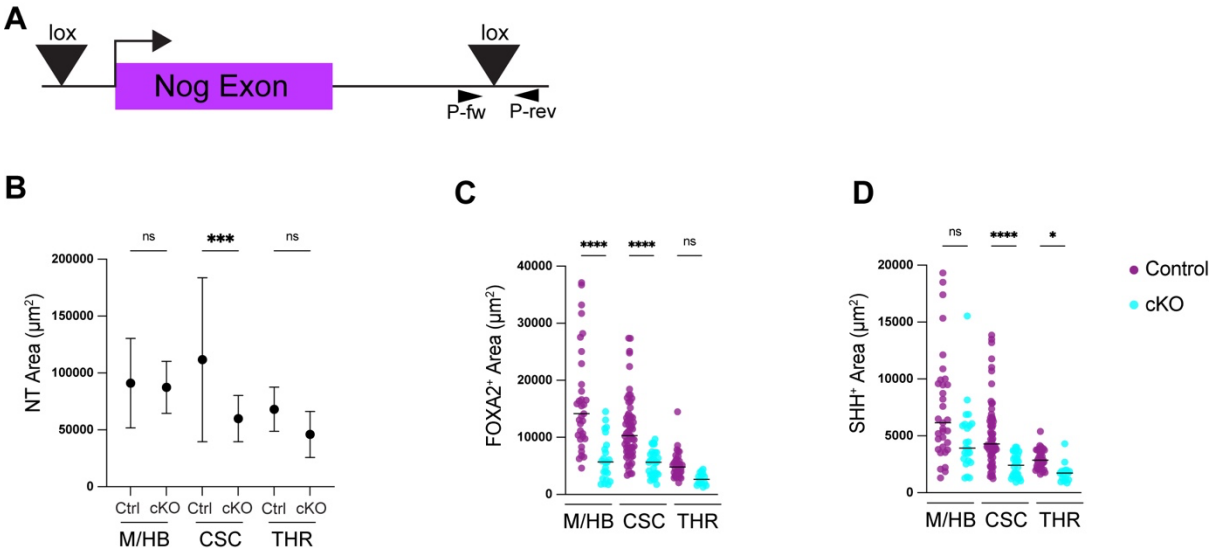

579

580 **Extended Figure S5: Characterisation of *Nog* cKO mouse.**

581 **A:** Schematic of *Nog* flox allele and the genotyping primers.

582 **B:** Total area of the NT measured by DAPI signal in serial sections from the different A-P
583 levels in of E10.5 Control ($Nog^{Fl/+};Sox2^{+/+}$ or $Nog^{Fl/Fl};Sox2^{+/+}$) and *Nog* cKO
584 ($Nog^{Fl/Fl};Sox2^{CreERT2/+}$) embryos of Mid/-Hindbrain (M/HB), Cervical spinal cord (CSC) and
585 Thorax (THR) embryos used to normalise the data in Figure 5C. The data is represented as
586 mean ± SD.

587 **C:** Raw area measurement of FOXA2 in sections from the different A-P levels corresponding
588 to analysis from Figure 5B and C. Kruskal-Wallis test and Dunn's multiple comparison tests
589 were performed between anatomical regions of Control vs *Nog* cKO (M/HB vs. M/HB p =
590 <0.0001, CSC vs. CSC p = <0.0001, THR vs. THR p = 0.0708).

591 **D:** Raw area measurement of SHH in different anatomical regions from the different A-P levels
592 corresponding to analysis from Figure 5B and C. Kruskal-Wallis test and Dunn's multiple
593 comparison tests were performed between anatomical regions of Control vs *Nog* cKO (M/HB
594 vs. M/HB p = 0.1129, CSC vs. CSC p = <0.0001, THR vs. THR p = 0.0431).

Materials & Methods

Cell culture

Maintenance

Mouse embryonic stem cells (ESC) were cultured in N2B27+2i+LIF (2iLIF) and incubated at 37°C in 5% CO_2. N2B27 medium comprised 1:1 DMEM/F-12 and Neurobasal (Gibco), 0.5% v/v N2 (Gibco), 1% v/v B27 (Gibco), 2 mM L-glutamine (Gibco), 1% penicillin/ streptomycin (Sigma), and 0.1 mM β-mercaptoethanol. To obtain 2iLIF medium, N2B27 was supplemented with 3 µM CHIR99021 (Tocris), 1 µM PD0325901 (Tocris) and 20 ng/ml murine LIF (Qkine). Tissue-culture treated 6-well plates were pre-coated with 0.15% gelatin (Sigma) in PBS at room temperature. Mouse ESCs were seeded at a density of 30,000 cells per 6-well, media was exchanged daily, and cells were passaged every third day by incubation with Accutase (Gibco) for 3 mins at 37°C, dissociation into single cells, centrifugation of the required number at 1500rpm for 5 mins, then re-seeding in a fresh well. R1 ESC line was used for most experiments and as the parental line for FOXA2-Venus reporter generation and for *Noggin* mutant (*Nog*^{mut}). HM1 ESC background was used as the parental line for *Shh* knock-out (*Shh*$^{-/-}$). Cell lines were routinely tested and confirmed negative for mycoplasma.

Generation of reporter cell lines

Generation of FOXA2-Venus reporter ESCs:

Foxa2-Venus Fusion (FVF) E-85 plasmid (kind gift from Heiko Lickert [47]) was used as a template for amplification of the FoxA2_exon3-venus-neo-PGK cassette, which was subsequently cloned into pGEMT-easy vector using Gibson Assembly technique. Two fragments for Gibson assembly were amplified using the E-085 vector as a PCR template:

1) Fragment1 - "FoxA2_exon3-Venus-Neo":

GibAs_p3_fwd: CGGCCGCGGGAATTCGATAAAGAATCAAAGACCAGTGGA

GibAs_p4_rev: GCCTCTCATTTCTACCGGGTAGGGGAGGCGCTTTT

2) Fragment 2 - "3' UTR-genomic DNA":

GibAs_p1_fwd: TCCCCTACCCGGTAGAAATGAGAGGCTGAGTGGAGACTTT

628 GibAs_p2_rev2:
629 CGCGAATTCACTAGTGATTCCCTCCTCCTTCAATTTCTCTTCCTTGTGTT
630
631 For CRISPR/Cas9 mediated knock-in of the Venus sequence at the 3' end of the FoxA2 gene
632 locus, gRNA3 (GCCTGCTAGCTCTGGTCACTG) was cloned into the pSpCas9(BB)-2A-
633 Puro (PX459) vector, containing the Cas9 sequence and a gRNA expression cassette. For
634 FoxA2 locus editing, both vectors were electroporated together into the ESC cell line R1 using
635 the Amaxa Nucleofector 4D, program CG-104. 24 hours after the electroporation, G418 (100
636 µg/ml) was added to the culture medium to select for positive clones. Single clones were
637 expanded, and correct integration of the Venus cassette was validated by PCR, sequencing and
638 standard Western blot analysis.
639 In brief, protein of cell lysates was obtained by directly adding 5xSample Buffer and boiling
640 samples at 95°C for 10 mins. The protein was loaded onto a NuPAGE™ 4-12% Bis-Tris gel
641 (Invitrogen) and run for 20 mins at 100V, then 90 mins at 150V, then proteins were blotted
642 onto a PROTRAN nitrocellulose transfer membrane (Whatman) by TE 77 Semi-Dry Transfer
643 Unit (Amersham). The membrane was blocked in 5% BSA in 1x Transfer Buffer (10x TB,
644 MeOH, H_2O) supplemented with Tween-20. Primary antibodies used: rabbit anti-FOXA2 (Cell
645 Signalling Technologies, #8186S, 1:1000) and mouse anti-ß-tubulin (MPI-CBG antibody
646 facility, 1:200).
647 FoxA2_fwd5: GACCTCAAGGCCTACGAACA
648 Venus_rev2: GTTGTGGCGGATCTTGAAGT (Product size: 694 bp)
649
650 *Generation of FoxA2-Venus and H2A-mCherry double-reporter ESCs:*
651 H2A-mCherry was integrated into the Rosa26 safe harbour locus of FOXA2-Venus cell line.
652 We first obtained a Rosa26 targeting vector with Puromycin selection cassette (pR26 CAG
653 AsiSI/MluI, Addgene 74286, Ralf Kuehn lab, [48]), linearized the vector with SwaI restriction
654 digest, and used Gibson assembly to insert the Gateway destination sequence immediately 3'
655 to the splice acceptor site, and created a new vector termed pR26-sA-DEST. Subsequently, we
656 performed a Gateway LR reaction between pR26-sA-DEST and pME-H2A-mCherry to create
657 pR26-sA-H2-mCherry. To edit the Rosa26 locus, we identified a new high efficiency guide
658 RNA sequence ACTGGAGTTGCAGATCACGA (Rosa26-gRNA1), and co-transfected p-
659 Rosa26-gRNA1 and pR26-sA-H2-mCherry to FoxA2-Venus cells with Amaxa nucleofection.
660 After 24 hours, cells were selected with 1 µg/ml Puromycin and individual clones were

661 expanded. Correct integration was confirmed by Sanger sequencing and the length of the PCR
662 amplicon from two primers:
663 R26_leftout_fwd1: GCTTGGTGCGTTTGCGGGGAT
664 mCherry_rev1: TTGGTCACCTTCAGCTTGGCG (Product size: 5943 bp)
665
666
667 **Generation of knockout mouse ESC lines by CRISPR/Cas9**
668
669 gRNAs were designed using the following tools:
670 https://portals.broadinstitute.org/gppx/crispick/public or https://www.vbc-score.org/
671
672 *Shh$^{-/-}$:*
673 A short guide RNA (sgRNA) sequence (GCTGCTGGTGTGCCCCGGGCTGG) was cloned
674 into pSpCas9(BB)-2A-Puro (PX459) V2.0 (Addgene plasmid #62988) as outlined in [49]. 2 µg
675 of PX459 V2.0 containing the sgRNA sequence were electroporated into 2x10^6 DVI2 ESCs
676 (HM1 background) using program A023 of the Amaxa Nucleofector II (Lonza) to ablate
677 endogenous *Shh* gene expression. Electroporated cells were seeded onto a gelatin coated 10cm
678 CellBind plate (Corning) and cultured in 2iLIF. The following day cells were treated with 1.5
679 µg/mL Puromycin (Sigma) for 48 hours. Cells were grown in 2iLIF until resistant colonies
680 were ready to be pick. Single and well spaced-out colonies were picked using a 20-µl pipette
681 tip, dissociated in 0.25% Trypsin (Gibco) and plated onto feeder cells in serum-containing ESC
682 medium + LIF in a 96-well plate to allow expansion. Colonies were screened and confirmed
683 for deletions via Sanger sequencing using primers ShhKOpFW
684 (CAAGCTCTCCAGCCTTGCTA) and ShhKOpRV (CTGCTCCCGTGTTTTCCTCA). The
685 11bp deletion caused a frameshift and premature stop codon. Cell lines were adapted back to
686 2iLIF conditions.
687
688 *Nog^{mut}:*
689 sgRNA2 (GGCGGATGTGTAGATAGTGCTGG) was cloned into the U6-IT-EF1As-Cas9-
690 P2A-GFP vector, containing the Cas9 sequence and a gRNA expression cassette. As described
691 previously, ESCs (R1) were electroporated with the construct using an Amaxa Nucleofector
692 4D (program CG-104). 40 hours post electroporation, single GFP$^+$ cells were analysed and
693 sorted based on their GFP expression relative to non-fluorescent control on a FACS Aria III
694 machine into individual wells of 96-well plates and clonal lines were expanded. One clone was

confirmed as trans-heterozygous mutant with a different sized deletion in each allele by PCR and sanger sequencing using the primers Nog_fwd1 TGAGGTGCACAGACTTGGAT and Nog_rev2 GCCGCCTTCCCAAGTAGA. CRISPR allele 1: large deletion followed by a frameshift and premature stop codon. 27 amino acids of NOGGIN protein remain, only corresponding to the signal peptide, followed by 21 out-of-frame amino acids. CRISPR allele 2: 33bp deletion including 8 amino acids of the signal peptide and 3 amino acids of NOGGIN.

Neural tube organoid (NTO) formation

ESCs were dissociated into single cells as described in "Maintenance". After centrifugation of the required number of ESCs in N2B27, the pellet was placed on ice then resuspended in Matrigel (Corning) to yield a suspension at 100 cells per µl of Matrigel. 45 µl of this suspension was spread evenly across a MatTek dish for FACS and RNA-seq experiments, or 4 µl of suspension was carefully distributed in the centre of an optical-bottom 96-well (PerkinElmer) for immunofluorescence experiments. Gellification was performed at 37°C for 15 mins (MatTek) or 4 min (96-well), then covered with pre-warmed N2B27 medium (2 ml per MatTek, or 100 µl per 96-well. "Standard" N2B27 medium for NTO generation was the same as the N2B27 base for 2iLIF (see "Maintenance"), with the addition of 1% sodium pyruvate (Gibco). "Advanced" N2B27 for making larger NTOs used Advanced DMEM/-12 (Gibco 12634-010 instead of 21331-020) and was supplemented with 1% v/v non-essential amino acids (Gibco). In both cases, medium was exchanged daily from Day 2 onwards. On Day 2, 250 nM all-trans RA (Sigma) was added to the N2B27 medium, then removed after 18 hours. For perturbations to NTOs, the following proteins or small molecules were added at the concentrations indicated in the corresponding figures: BMP4 (Gibco), BMP7 (Gibco), LDN (Selleck Chemicals), NOGGIN (R&D), CHIR99021 (Tocris), IWP2 (Selleck Chemicals), IWR-1endo (Sigma), FGF2 (PeproTech), FGF8b (in house), or PD0325901 (Tocris).

722 ## Immunofluorescence

723

724 **Wholemount staining of NTOs**

725

726 NTOs were fixed in 2% PFA for 30 min at room temperature, by adding 1:1 volume of room
727 temperature 4% PFA on top of culture media, to avoid Matrigel disintegration. After fixation,
728 samples were washed three times in PBS, then blocked and permeabilised in b/p buffer (PBS,
729 1% BSA, 0.5% Triton X-100) for 24 hours at 4°C. Primary antibodies were applied in b/p
730 buffer for 24-72 hours at 4°C to ensure deep penetration of the samples: LEF1 (Cell Signalling
731 Technologies, #2230S, 1:200), FOXA2 (R&D, #AF2400, 1:400), FOXA2 (Cell Signalling
732 Technologies, #8186S, 1:1000), NKX6.1 (DSHB, #F55A10s, 1:200). Samples were washed
733 three times and for a total of at least 24 hours in b/p at 4°C, then incubated with Alexa Fluor
734 conjugated secondary antibodies (Invitrogen Donkey anti-Mouse/Goat/Rabbit 1:400) and
735 DAPI (Sigma) for 24-72 hours at 4°C. Finally, samples were washed then stored in PBS.

736

737 The following primary antibodies were also used with modifications to the fixation and staining
738 procedures. For SHH (Cell Signalling Technologies, #2207S, 1:300), antigen retrieval with 1x
739 citrate buffer (DAKO) was performed for 45 mins at 65°C prior to blocking and
740 permeabilization. For pSMAD1/5/9 (Cell Signalling Technologies, #13820S, 1:800), fixation
741 was performed in EMgrade PFA (Electron Microscopy Sciences) (8% diluted to a 2% final
742 concentration) (12mins for 4µl Matrigel at room temperature). For both pSMAD1/5/9 and
743 pERK (Cell Signalling Technologies, #4370S, 1:500), after fixation samples were
744 permeabilised with methanol for 10 mins at -20°C, then blocked in db/p (PBS, 5% donkey
745 serum, 0.3% Triton X-100) at 4°C.

746

747

748 **Optical clearing of wholemount NTOs**

749

750 PBS was removed and CUBIC-R+(N) refractive index matching solution [50] was added to
751 completely cover the samples and incubated for 30-60 min at RT. After this adaptation,
752 CUBIC-R+(N) solution was exchanged to fresh CUBIC-R+(N) supplemented with 2 mg/ml
753 propylgallate (Sigma) to reduce photobleaching.

754 **Staining of embryo sections**

755

756 E10.5 embryos were fixed on ice for 75 mins in 4% PFA, washed in PBS, then adapted to
757 sucrose and embedded in gelatin prior to cryosectioning. Slides were washed 3x for 15 mins
758 each in 41°C PBS to dissolve the gelatin. Afterwards, slides underwent antigen retrieval as per
759 SHH staining protocol above, then were blocked for 1 hour at room temperature in b/p. Primary
760 antibodies as above were incubated overnight at 4°C in a humidified chamber. Samples were
761 washed 3x for 5 mins with PBS+0.3% Triton X-100 at room temperature. Secondary antibodies
762 were applied in a concentration of 1:200 in b/p and incubated overnight at 4°C. Samples were
763 washed 3x for 5 mins with PBS+0.3% Triton X-100 at room temperature, then mounted in
764 ProLong Diamond Antifade Mountant.

765

766

767 **Imaging**

768

769 **Viventis lightsheet live-imaging**

770

771 ESCs were dissociated and seeded as described in "Neural tube organoid (NTO) formation",
772 but at a density of 80 cells/µl Matrigel in special Viventis chambers, lined with FEP film from
773 inside. Chambers were manufactured manually by gluing the FEP sheet to the plastic chambers
774 and left to dry overnight. Chambers were cleaned with plasma to reduce hydrophobic properties
775 and facilitate the attachment of the Matrigel. Before use, chambers were washed 3x with water
776 and 80% ethanol, and dried and sterilised under UV light for at 1 hour at room temperature.

777

778 After seeding and gellification of 40 µl Matrigel, 1.5 ml of N2B27 medium was added to the
779 chamber and exchanged daily from Day 2. Live-imaging was initiated from Day 3 of the NTO
780 generation procedure, i.e. 6 hours after RA removal, over a timecourse of 48-75 hours. Samples
781 were incubated at 37°C in 5% CO_2 with humidification throughout. Images were acquired using
782 two Nikon 10x objectives (NA 0.3) for illumination and for detection one Nikon 25x (NA 1.1)
783 water immersion objective with 18x magnification and imaged with the following settings:
784 mCherry 50 ms exposure time, 0.5% laser power; Venus 10 ms exposure time, 3.5% laser
785 power. Multiple NTOs at different *xyz* positions were imaged at each timepoint. Image
786 acquisition was performed in stacks with 3 µm step size every 15 mins.

787 **Spinning disk fixed sample imaging**

788

789 Wholemount NTOs and embryo sections were imaged on a Spinning Disk Confocal Olympus
790 (inverted) microscope using a 10x (NA 0.4) air objective. Lasers were used at 100% and
791 exposure time was adjusted to 200 ms for all lasers. Resolution was 0.65 µm in *x* and *y*. For
792 wholemount NTOs, 125 planes with 2 µm spacing in *z* were acquired to allow for 3D
793 reconstruction, and an automated stage was used for high-throughput acquisition with unbiased
794 selection of multiple positions per 96-well using a grid. For embryo sections, planes with 2 µm
795 spacing in *z* were acquired. For von Mises-Fisher analyses, fixed NTO images were acquired
796 on the same microscope but using a 40x (NA 1.25) silicon oil objective, with 0.57 µm spacing
797 in *z*.

798

799

800 **Image processing and quantification**

801

802 The transition from the scattered FOXA2^{+} state to the intermediate clustered state was scored
803 manually in Figures 1D and 2C-F. The transition is heterogeneous from NTO to NTO, and the
804 tissue contains a high density of nuclei, so it was difficult to apply standardised parameters for
805 automated image analysis. During manual analysis, a cluster was defined as at least three cells
806 that were grouped together and displayed nuclear signal intensity of a minimum of 15% of Day
807 5 FOXA2 signal intensity.

808

809 Automated analyses were performed for Figures 1C, 4C, 4E-F, S1B, S3C and S4C-E as
810 described below.

811

812

813 **Analysis of Viventis movies**

814

815 As mentioned above, manual classification was performed to analyse data in Figure 2C-F. to
816 avoid biases, two people analysed two different datasets and confirmed findings from two
817 different microscope methods with the same conclusion.

818

819 For intensity quantification of clusters over time in Figure 2D (right panel), we used maximum
820 intensity *z*-projections, performed intensity-based thresholding for segmentation, and
821 quantified the total FOXA2$^+$ intensity for each cluster for individual frames with a Python
822 script using scikit-image library. The movies were manually inspected from an orthogonal view
823 in the *x*, *z* plane to ensure that there were no clusters overlapping in the *z*-direction.
824
825 For presentation, representative maximum intensity *z*-projections were made in ImageJ, or
826 movies were exported as .mp4 files.
827
828
829 **Analysis of fixed wholemount NTO images**
830
831 Raw .vsi files were processed in ImageJ. For presentation, single representative *z* slices were
832 exported as .tif files with set display ranges for each channel and without any binning in *x*-*y*.
833
834 *von Mises-Fisher analysis:*
835 Imaris software was used to 3D reconstruct and visualise each NTO. FOXA2$^+$ nuclei above a
836 set intensity threshold were identified using the spots function in Imaris and applied as a batch
837 script. The precision of automated FOXA2$^+$ nucleus identification was checked and corrected
838 manually. The geometric centre of the inscribed spot was considered the geometric centre of
839 each nucleus and their *x, y*, *z* coordinates were used to calculate the concentration parameter,
840 *k*, as the resulting vector calculated as a sum of all vectors built from the centre of the NTO to
841 the centre of each FOXA2$^+$ nucleus and normalised to the number of FOXA2$^+$ nuclei.
842
843 *Correlation analysis of FOXA2 vs LEF1, pERK, pSMAD1/5/9 signal intensities in NTOs:*
844 To analyse the spatial correlation of FOXA2 and signalling pathways, we used images of fixed
845 NTOs prepared and acquired on the spinning disc microscope as described above. For each
846 NTO, we used ImageJ to visually determine the midsagittal plane, draw a curved path with
847 linewidth of 10 pixel within the tissue, measured the intensities of different channels along this
848 path, and exported the results. Then, we used a Python script to calculate the Pearson
849 correlation between the FOXA2 channel and a second channel representing LEF1, pERK, or
850 pSMAD1/5/9. In this way, we obtained a single Pearson correlation per NTO.
851
852

853 *3D quantification of NTO features:*

854 For 3D image analysis, we first processed the raw .vsi files to isotropic .tif files using CLIJ [51].
855 GPU-accelerated image processing library in ImageJ. Due to the "fish-bowl" effect of CUBIC-
856 R+(N)'s high refractive index (RI = 1.5), the effective *z* steps were 3 μm. We therefore binned
857 images in *x*-*y* from to 0.65 μm to 3 μm so that the 3D voxel dimensions were comparable
858 (3 μm × 3 μm × 3 μm in the *x*, *y* and *z* directions).

859 To quantify FOXA2$^+$ cluster number per NTO in 3D (Figures 4C, 4E, S4D-E), we used
860 CellProfiler 4 [52]. First, we segmented the NTO outer boundary by applying Otsu thresholding
861 to the *z* stacks from the DAPI channel. Then, we segmented FOXA2$^+$ clusters by applying a
862 set intensity threshold to the *z* stacks from the FOXA2 channel and assigned these "child"
863 clusters to their "parent" NTO. The FOXA2 intensity threshold was determined by comparison
864 between positive control RA-treated versus negative control untreated endpoint NTOs and
865 applied equally across all samples from the same experiment.

866

867 For scoring whether NTOs expressed any FOXA2, NKX6.1 and/or SHH (Figure 1C, S1B,
868 S3C), the mean intensity of the corresponding channel was measured inside the DAPI
869 segmented volume. To measure the size of NTOs (Figure S4C, S4E), the NTO surface area
870 was inferred from the DAPI segmented volume assuming spherical shape and to overcome
871 confounding crenulation of the mask surface.

872

873 *Measurement of FOXA2$^+$ cluster size:*

874 The quantification of FOXA2$^+$ cluster properties for fixed NTOs shown in Figure 4F was
875 generated using a combination of discrete geometry and computer vision techniques. First,
876 down-sampled multi-channel image volumes were processed in Ilastik [53] to produce a high
877 contrast segmentation of NTOs from background. Surface reconstruction methods contained
878 in the TubULAR package [54] were then applied to these processed image volumes in order to
879 build mesh triangulations approximating the epithelial mid-surface of each NTO. FOXA2
880 signal intensity on each mesh surface was quantified by sampling the image volume at subpixel
881 resolution onto mesh triangles and then using angle-weighted averaging to compute a single
882 intensity value for each mesh vertex.

883

884 FOXA2$^+$ clusters were identified on a per-vertex basis using a custom consensus clustering
885 algorithm, which produces a single "best" clustering by comparing results across an ensemble
886 of input clusterings. Prior to clustering, the FOXA2 intensity on each vertex was normalised

between [0,1] by a linear re-scaling between the 5th and 95th percentiles of all raw intensities measured on WT NTO given RA treatment. A single clustering in the ensemble was generated by assigning an index to each vertex in the surface mesh using a modified k-means method. Given a set of random initial cluster centres, a modified version of Lloyd's algorithm was used to greedily minimise the following cost function:

$$C[\{\vec{c}\}, f_B] = \frac{1}{\sum_v a_v f_v}\left(\sum_{\vec{c_i}\in\{\vec{c}\}}\sum_{v\in\vec{c_i}} \frac{d^2(\vec{x_v},\vec{c_i})}{D_{max}^2}\ a_v f_v + \alpha \sum_{v\in B}(f_v - f_B)^2\ a_v f_v\right),$$

where $\{\vec{c}\}$ denotes the set of all cluster centers, , f_B is the average FOXA2 intensity of the background, a_v is the barycentric area of vertex v, f_v is the normalised FOXA2 intensity on vertex $v, \vec{x_v}$ is the 3D location of vertex $v, d(\vec{x}, \vec{y})$ denotes the 3D Euclidean distance between two points $\vec{x}$ and $\vec{y}$ on the surface, D_{max} is the maximum distance between any two points on the NTO's surface, and α is a positive scalar that sets the relative weight of the foreground versus background terms in the cost function. The double sum in the first term runs over all vertices v associated to each cluster centre ($\vec{c_i} \in \{\vec{c}\}$. The sum in the second term runs over all vertices assigned to the background. A vertex v was assigned to cluster $\vec{c_i}$ if

$$d^2(\vec{x_v}, \vec{c_i}) < d^2(\vec{x_v}, \vec{c_j})\ \forall\, i \neq j \quad \text{and} \quad d^2(\vec{x_v}, \vec{c_i}) < D_{max}^2\, \alpha\, (f_v - f_B)^2,$$

or alternatively to the background if

$$D_{max}^2\, \alpha\, (f_v - f_B)^2 < d^2(\vec{x_v}, \vec{c_i})\ \forall\, \vec{c_i} \in \{\vec{c}\}\,.$$

Intuitively, the cost function $C[\{\vec{c}\}, f_B]$ is minimised when all points in the background have similar (low) intensities and all foreground points are assigned to a nearby cluster centre. Given an ensemble of such clusterings, the method of [55] was used to produce a consensus clustering that is as close as possible to all the individual clusterings in the ensemble (formally it is the Fréchet sample mean of the clustering ensemble). The consensus clustering was then post-processed to ensure that each FOXA2$^+$ cluster was simply connected. The use of a consensus clustering algorithm obviates the dependence of the output on the initial locations of the randomly chosen cluster centres. For our analysis, we set $\alpha = 1$ and used 10 initial cluster centres to generate each element of the clustering ensemble. The initial background intensity was always taken to the lowest intensity on the surface. Numerical experiments showed that the choice of $d(\vec{x}, \vec{y})$ to be the 3D Euclidean distance produced indistinguishable results from more sophisticated methods using exact geodesic distances on the surface[56] after consensus clustering. Total FOXA2$^+$ surface area for a given NTO was taken to be the sum of all barycentric areas associated to each mesh vertex assigned to any FOXA2$^+$ cluster, then the mean FOXA2$^+$ surface area per cluster was computed based on the number of FOXA2$^+$ clusters identified for each NTO.

920 **Analysis of embryo sections**

921

922 For area measurements of FOXA2 and SHH in embryo sections, we first converted raw .vsi
923 files to maximum intensity z-projections in ImageJ. We set all channels to auto intensity and
924 used the freehand selection tool from ImageJ to outline 1) the outer edge of the NT based on
925 DAPI staining, 2) the NT lumen, 3) FOXA2 signal, and 4) SHH signal, and measured area in
926 μm^2. To get the actual area of the NT, we subtracted 1) NT area by 2) lumen area. To get the
927 normalised area measurements of FOXA2 and SHH respectively, we divided the area
928 measurement of the signal 3) or 4) by the NT area. For presentation, maximum intensity *z*-
929 projections with set display ranges were used. We analysed 6 control and 3 cKO embryos from
930 two litters.

931

932

933 **RNA sequencing**

934

935 RNA-seq data generated in this study are available at the Gene Expression Omnibus (GEO)
936 under accession codes GSExxxxxx (FOXA2$^+$ vs FOXA2$^-$ cells at Day 5, Figure 3) and
937 GSExxxxxx (FOXA2$^+$ vs FOXA2$^-$ cells after BMP perturbations, Figure 4).

938

939

940 **RNA-seq of RA-treated vs untreated timecourse from Day 2-5, Figure S1**

941

942 Timecourse RNA-seq data [19] was obtained from GEO with accession code GSE214368. In
943 brief, RNA-seq reads were trimmed using Trim Galore v0.5.0, filtered to remove abundant
944 sequences using Bowtie 2 v2.3.4.1, aligned to the GRCm38 genome (Ensembl release 94) using
945 STAR v2.6.0c and summarised per gene with featureCounts (subread v1.6.2). Further analysis
946 was performed using DESeq2 v1.18.1.

947 **RNA-seq of FOXA2$^+$ vs FOXA2$^-$ cells at Day 5, Figure 3**

948

949 RA-treated NTOs were extracted from Matrigel, dissociated into single cell suspension and
950 FACS sorted into two cell populations based on FOXA2-Venus expression relative to non-
951 fluorescent control on a FACS Aria III machine. For each sample, produced in three biological
952 replicates, a minimum of 50,000 cells was sorted for subsequent RNA extraction. RNA was
953 extracted from sorted cells using QIAGEN RNeasy Micro Kit and then underwent library
954 preparation using the NEBNext Poly(A) mRNA Magnetic Isolation Module (E7490) and the
955 NEBNext Ultra Directional RNA Library Prep Kit for Illumina (E7420), and bulk RNA
956 sequencing on an Illumina NextSeq500 (single-end reads 75 bp).

957

958 RNA-seq reads were trimmed using Trim Galore v0.5.0, filtered to remove abundant sequences
959 using Bowtie 2 v2.3.4.1, aligned to the GRCm38 genome (Ensembl release 94) using STAR
960 v2.6.0c and summarised per gene with featureCounts (subread v1.6.2). Further analysis was
961 performed using DESeq2 v1.18.1 and activated and inhibited upstream regulators were
962 predicted using IPA Upstream Regulator Analysis based on the differentially expressed genes.
963 Differentially expressed genes (DEG) of FOXA2$^+$ versus FOXA2$^-$ samples at a false discovery
964 rate (FDR) threshold of 5% were subjected to IPA Upstream Regulator Analysis for predicting
965 activated and inhibited upstream regulators. In addition, top 400 DEGs ranked by padj were
966 used in gene set over-representation analysis with clusterprofiler 4.6.2 and GO.db 3.16.0.

967

968

969 **RNA-seq of FOXA2$^+$ vs FOXA2$^-$ cells after BMP perturbations, Figure 4**

970

971 NTOs were treated with RA at Day 2 for 18 hours as usual. At Day 3, i.e. 6 hours after RA
972 removal, BMP4 (1.5 ng/ml) or LDN (100 nM) was added for 8 hours. To harvest cells, NTOs
973 were washed twice with ice cold PBS, then dissociated in TryplE. FOXA2-Venus$^+$ or FOXA2-
974 Venus$^-$ cells were FACS sorted into lysis buffer in a 96-well plate, with 100 cells sorted for
975 each sample in triplicate, then snap frozen on dry ice. RNA was extracted and sequencing
976 libraries were prepared following the TM3'seq protocol [57] for subsequent quantitative
977 sequencing with enrichment for polyadenylated RNAs. Pooled libraries were sequenced on the
978 Illumina NovaSeq S4 PE150 (paired-end 500bp reads).

979

980 The paired-end raw reads were first split and the 12bp of UMI were extracted from read2 with
981 UMI-tools (v1.0.0). Reads were then trimmed with Cutadapt (v1.18) and mapped to the mouse
982 genome (mm10) using STAR (v2.5.2a). UMI counts at gene levels were quantified by HTSeq
983 (v0.11.2). The normalised counts per million (cpm) were obtained with DESeq2 (v1.26.0).
984
985
986 **Mouse procedures**
987
988 Mouse procedures were approved under the license BMWFW-66.018/0006-WF/V/3b/2016
989 ("Coordination of tissue growth and patterning in neural tube development") from the Austrian
990 Bundesministerium für Wissenschaft, Forschung und Wirtschaft and performed in accordance
991 with the relevant regulations. The following strains were previously described: *Sox2*^{CreERT2} [23],
992 *Nog*$^{Fl/+}$ [22]. To conditionally delete Noggin, *Nog*$^{Fl/+}$ were bred to *Sox2*^{CreERT2} mice to generate
993 *Nog*$^{Fl/Fl}$, *Sox2*$^{CreERT2/+}$ embryos. Pregnant mothers were intraperitoneally injected with 4mg
994 tamoxifen in sunflower oil per mouse at embryonic Day E5.5. Embryos were harvested at
995 E10.5. The expected ratios of genotypes were obtained.
996
997
998 **Genotyping**
999
1000 Lysates for PCR were prepared following the HotSHOT protocol [58]. Briefly, yolk sacs were
1001 transferred to clean tubes and lysed in Alkaline lysis reagent (25 mM NaOH, 0.2 mM disodium
1002 EDTA, pH 12) at 95°C for approx. 45 min. After cooling samples to 4°C, 1x volume of
1003 Neutralization buffer (40 mM Tris-HCl, pH5) was added to stop the lysis reaction. 2 µl of
1004 lysate was used in a 20 µl PCR reaction. To genotype the *Nog*^{FL}, Primers Nog F 13351 (CCA
1005 CAA TAT CCA GCC CTT GT) and Nog R 13352 (AAG AGG CCC ATG TGA GTG TC)
1006 were used to detect the floxed allele. 10 µl PCR product was loaded onto a 2% gel and run at
1007 110 Volt for 30 min. The WT band was 186bp, the mutant band 300bp. To genotype the
1008 *Sox2*^{CreERT2}, primers 344 (GTCCAATTTACTGACCGTACACC) and 345
1009 (GTTATTCGGATCATCAGCTACACC), as well as the internal control primers OIMR0042
1010 (CTAGGCCACAGAATTGAAAGATCT) and OIMR0043
1011 (GTAGGTGGAAATTCTAGCATCATCC) were used. The Mutant band was 705bp, the
1012 Internal Control 324bp.

1013 # Data representation & availability

1014

1015 Data of this study are presented as follows. Bar-plots with error bars showing standard
1016 deviation (SD): Figures 1C, 1E, 2E, 4C, 4E, 4I, S1B, S3C, S4D. Box-plots with median
1017 represented as centre line, whiskers show range of values, dots (if present) represent all
1018 measurement points: Figures 1F, 3E, S1C, S4C, S4E. Scatter dot-plots with mean represented
1019 as centre line (or dot) and error bars showing standard deviation (SD): Figures 4F, 5C, S5B,
1020 S5C. Asterisks indicate statistical significance, n.s. indicates non-significance.

1021

1022

1023 **Data availability**

1024

1025 RNA-seq data generated in this study have been deposited at GEO under accession codes
1026 GSExxxxxx (FOXA2^{+} vs FOXA2^{-} cells at Day 5, Figure 3) and GSExxxxxx (FOXA2^{+} vs
1027 FOXA2^{-} cells after BMP perturbations, Figure 4).

1028

1029 Primers and oligonucleotide sequences are available in the Materials & Methods section.

1030 # Supplementary files provided

1031

1032 **Supplementary Movies 1-2**

1033 Live-imaging of RA-treated NTO showing FOXA2 self-organisation from Day 3-5.
1034 Maximum intensity *z*-projections of H2A-mCherry (magenta) and FOXA2-Venus (green)
1035 merged (Movie 1) or FOXA2-Venus (green) single channel (Movie 2) are represented as
1036 movies, related to Figure 2C.

1037

1038 **Supplementary Movies 3-4**

1039 Live-imaging of RA-treated NTO showing FOXA2 self-organisation from Day 3-5.
1040 Maximum intensity *z*-projections of H2A-mCherry (magenta) and FOXA2-Venus (green)
1041 merged (Movie 3) or FOXA2-Venus (green) single channel (Movie 4) are represented as
1042 movies, related to Figure 2D, Extinction.

1043

1044 **Supplementary Movies 5-6**

1045 Live-imaging of RA-treated NTO showing FOXA2 self-organisation from Day 3-5.
1046 Maximum intensity *z*-projections of H2A-mCherry (magenta) and FOXA2-Venus (green)
1047 merged (Movie 5) or FOXA2-Venus (green) single channel (Movie 6) are represented as
1048 movies, related to Figure 2D, Sorting.

Author contributions

T.K., H.T.S., and E.G. designed and performed experiments, created methodologies, and analysed the data. K.I. provided supervision, set up live imaging conditions, developed image analysis pipelines and helped analysing data. D.C. and E.S. developed image analysis pipelines. M.M. and J.B. generated *Shh*$^{-/-}$ ESCs. J.W. performed bioinformatic analyses. E.C. and L.A. performed experiments. S.L. and A.K. provided *Nog* cKO embryos. A.H. and R.N. assisted with pharmacological screen. N.E. supported development of larger NTO media. H.T.S., T.K. and E.M.T. wrote the manuscript. E.M.T. conceived and supervised the study.

Acknowledgements

We thank P. Pasierbek, A. C. Moreno, T. Lendl and K. Aumayr for microscopy support, G. Schmauss for FACS support, M. Novatchkova for assistance with Bioinformatic analyses, J. Ahel, S. Horer, E. Cesare, E. Norouzi for technical assistance, A. Meinhardt for supervision, DRESDEN-concept Genome Center, A. Vogt and the Vienna Biocentre NGS facility for RNA sequencing. We are grateful to M. Placzek and E. Martí for discussion about the floorplate, to S. Shvartsman for valuable input, to A. Aszodi, W. Masselink and S. Raiders for advice on statistical analyses, to J. Cornwall Scoones, G. Martello and Tanaka lab members for critical reading of the manuscript, E. Bassat and E. Chatzidaki for contributing schematics, and to K. Lust for support. The work was supported by funding from the Austrian Science Fund (FWF): F7803-B (Stem Cell Modulation) to E.M.T. and A.K, WWTF 10.47379/LS17037 and ERC AdG 742046 to E.M.T., Sir Henry Wellcome postdoctoral fellowship to H.T.S., ELBE fellowship to K.I., National Science Foundation (US) Phy 2013131 to E.S.. The A.K. lab is also supported by ISTA, the European Research Council under Horizon Europe grant 101044579, and S.L. is supported by Gesellschaft für Forschungsförderung Niederösterreich m.b.H. fellowship SC19-011. This work was supported in part by the Francis Crick Institute which receives its core funding from Cancer Research UK (CC001051), the UK Medical Research Council (CC001051), and the Wellcome Trust (CC001051). For the purpose of Open Access, the authors have applied a CC BY public copyright license to any Author Accepted Manuscript (AAM) version arising from this submission.

1081 # Declaration of interests

1082

1083 AH and RAN are full time employees of Boehringer Ingelheim RCV.

1084 # References

1085

1086 1. Spemann, H. & Mangold, H. über Induktion von Embryonalanlagen durch Implantation
1087 artfremder Organisatoren. *Arch. Für Mikrosk. Anat. Entwicklungsmechanik* **100**, 599–638
1088 (1924).
1089 2. Gurdon, J. B. Embryonic induction — molecular prospects. *Development* **99**, (1987).
1090 3. Martinez Arias, A. & Steventon, B. On the nature and function of organizers. *Dev. Camb.*
1091 *Engl.* **145**, dev159525 (2018).
1092 4. Sato, T. *et al.* Single Lgr5 stem cells build crypt-villus structures in vitro without a
1093 mesenchymal niche. *Nature* **459**, 262–265 (2009).
1094 5. Eiraku, M. *et al.* Self-organizing optic-cup morphogenesis in three-dimensional culture.
1095 *Nature* **472**, 51–56 (2011).
1096 6. Meinhardt, A. *et al.* 3D Reconstitution of the Patterned Neural Tube from Embryonic
1097 Stem Cells. *Stem Cell Rep.* **3**, 987–999 (2014).
1098 7. Martyn, I., Kanno, T. Y., Ruzo, A., Siggia, E. D. & Brivanlou, A. H. Self-organization of
1099 a human organizer by combined Wnt and Nodal signaling. *Nature* **558**, 132–135 (2018).
1100 8. Bikoff, J. B. *et al.* Spinal Inhibitory Interneuron Diversity Delineates Variant Motor
1101 Microcircuits. *Cell* **165**, 207–219 (2016).
1102 9. Sagner, A. & Briscoe, J. Establishing neuronal diversity in the spinal cord: A time and a
1103 place. *Development (Cambridge)* vol. 146 (2019).
1104 10. Dessaud, E., McMahon, A. P. & Briscoe, J. Pattern formation in the vertebrate neural
1105 tube: a sonic hedgehog morphogen-regulated transcriptional network. *Development* **135**,
1106 2489–2503 (2008).
1107 11. Le Dréau, G. & Martí, E. Dorsal-ventral patterning of the neural tube: A tale of three
1108 signals. *Dev. Neurobiol.* **72**, 1471–1481 (2012).
1109 12. Jessell, T. M. Neuronal specification in the spinal cord: inductive signals and
1110 transcriptional codes. *Nat. Rev. Genet.* **1**, 20–29 (2000).
1111 13. Yamada, T., Placzek, M., Tanaka, H., Dodd, J. & Jessell, T. M. Control of cell pattern in
1112 the developing nervous system: Polarizing activity of the floor plate and notochord. *Cell*
1113 **64**, 635–647 (1991).
1114 14. Patten, I., Kulesa, P., Shen, M. M., Fraser, S. & Placzek, M. Distinct modes of floor plate
1115 induction in the chick embryo. *Development* **130**, 4809–4821 (2003).

1116 15. Placzek, M., Tessier-Lavigne, M., Yamada, T., Jessell, T. & Dodd, J. Mesodermal
1117 Control of Neural Cell Identity: Floor Plate Induction by the Notochord. *Science* **250**,
1118 985–988 (1990).
1119 16. Placzek, M. & Briscoe, J. The floor plate: multiple cells, multiple signals. *Nat. Rev.*
1120 *Neurosci.* **6**, 230–240 (2005).
1121 17. Kremnyov, S., Henningfeld, K., Viebahn, C. & Tsikolia, N. Divergent axial
1122 morphogenesis and early shh expression in vertebrate prospective floor plate. *EvoDevo* **9**,
1123 1–17 (2018).
1124 18. Ranga, A. *et al.* Neural tube morphogenesis in synthetic 3D microenvironments. *Proc.*
1125 *Natl. Acad. Sci.* **113**, (2016).
1126 19. Ishihara, K. *et al.* Topological morphogenesis of neuroepithelial organoids. *Nat. Phys.*
1127 (2022) doi:10.1038/s41567-022-01822-6.
1128 20. Sasaki, H., Hui, C., Nakafuku, M. & Kondoh, H. A binding site for Gli proteins is
1129 essential for *HNF-3* β floor plate enhancer activity in transgenics and can respond to Shh
1130 in vitro. *Development* **124**, 1313–1322 (1997).
1131 21. Etoc, F. *et al.* A Balance between Secreted Inhibitors and Edge Sensing Controls
1132 Gastruloid Self-Organization. *Dev. Cell* **39**, (2016).
1133 22. Stafford, D. A., Brunet, L. J., Khokha, M. K., Economides, A. N. & Harland, R. M.
1134 Cooperative activity of noggin and gremlin 1 in axial skeleton development.
1135 *Development* **138**, 1005–1014 (2011).
1136 23. Arnold, K. *et al.* Sox2+ Adult Stem and Progenitor Cells Are Important for Tissue
1137 Regeneration and Survival of Mice. *Cell Stem Cell* **9**, 317–329 (2011).
1138 24. Balmer, S., Nowotschin, S. & Hadjantonakis, A.-K. Notochord morphogenesis in mice:
1139 Current understanding & open questions: Notochord Morphogenesis in Mice. *Dev. Dyn.*
1140 **245**, 547–557 (2016).
1141 25. Turing, A. M. The chemical basis of morphogenesis. *Philos. Trans. R. Soc. Lond. B. Biol.*
1142 *Sci.* **237**, 37–72 (1952).
1143 26. Gierer, A. & Meinhardt, H. A theory of biological pattern formation. *Kybernetik* **12**, 30–
1144 39 (1972).
1145 27. Zheng, Y. *et al.* Dorsal-ventral patterned neural cyst from human pluripotent stem cells in
1146 a neurogenic niche. *Sci. Adv.* **5**, eaax5933 (2019).
1147 28. Abdel Fattah, A. R. *et al.* Actuation enhances patterning in human neural tube organoids.
1148 *Nat. Commun.* **12**, (2021).

1149 29. Abdel Fattah, A. R. *et al.* Neuroepithelial Organoid Patterning is Mediated by Wnt-
1150 Driven Turing Mechanism. *bioRxiv* (2021) doi:10.2139/ssrn.3811873.
1151 30. Lancaster, M. A. *et al.* Cerebral organoids model human brain development and
1152 microcephaly. *Nature* **501**, 373–379 (2013).
1153 31. Van Den Brink, S. C. *et al.* Symmetry breaking, germ layer specification and axial
1154 organisation in aggregates of mouse embryonic stem cells. *Development* **141**, 4231–4242
1155 (2014).
1156 32. Takata, N., Sakakura, E., Eiraku, M., Kasukawa, T. & Sasai, Y. Self-patterning of rostral-
1157 caudal neuroectoderm requires dual role of Fgf signaling for localized Wnt antagonism.
1158 *Nat. Commun.* **8**, 1339 (2017).
1159 33. Rivron, N. C. *et al.* Blastocyst-like structures generated solely from stem cells. *Nature*
1160 **557**, (2018).
1161 34. Turner, D. A., Baillie-Johnson, P. & Martinez Arias, A. Organoids and the genetically
1162 encoded self-assembly of embryonic stem cells. *BioEssays* **38**, 181–191 (2016).
1163 35. McNamara, H. M., Solley, S. C., Adamson, B., Chan, M. M. & Toettcher, J. E.
1164 *Recording morphogen signals reveals origins of gastruloid symmetry breaking*.
1165 http://biorxiv.org/lookup/doi/10.1101/2023.06.02.543474 (2023)
1166 doi:10.1101/2023.06.02.543474.
1167 36. Suppinger, S. *et al.* Multimodal characterization of murine gastruloid development. *Cell*
1168 *Stem Cell* **30**, 867-884.e11 (2023).
1169 37. Simunovic, M. *et al.* A 3D model of a human epiblast reveals BMP4-driven symmetry
1170 breaking. *Nat. Cell Biol.* **21**, 900–910 (2019).
1171 38. Shao, Y. *et al.* A pluripotent stem cell-based model for post-implantation human amniotic
1172 sac development. *Nat. Commun.* **8**, 208 (2017).
1173 39. Mori, S. *et al.* Self-organized formation of developing appendages from murine
1174 pluripotent stem cells. *Nat. Commun.* **10**, 3802 (2019).
1175 40. Serra, D. *et al.* Self-organization and symmetry breaking in intestinal organoid
1176 development. *Nature* **569**, 66–72 (2019).
1177 41. Le Dréau, G. *et al.* Canonical BMP7 activity is required for the generation of discrete
1178 neuronal populations in the dorsal spinal cord. *Development* **139**, 259–268 (2012).
1179 42. Lee, K. J., Dietrich, P. & Jessell, T. M. Genetic ablation reveals that the roof plate is
1180 essential for dorsal interneuron specification. *Nature* **403**, 734–740 (2000).

1181 43. Lee, K. J., Mendelsohn, M. & Jessell, T. M. Neuronal patterning by BMPs: a requirement
1182 for GDF7 in the generation of a discrete class of commissural interneurons in the mouse
1183 spinal cord. *Genes Dev.* **12**, 3394–3407 (1998).
1184 44. Dale, K. *et al.* Differential patterning of ventral midline cells by axial mesoderm is
1185 regulated by BMP7 and chordin. *Development* **126**, 397–408 (1999).
1186 45. McMahon, J. A. *et al.* Noggin-mediated antagonism of BMP signaling is required for
1187 growth and patterning of the neural tube and somite. *Genes Dev.* **12**, 1438–1452 (1998).
1188 46. Furuta, Y., Piston, D. W. & Hogan, B. L. M. Bone morphogenetic proteins (BMPs) as
1189 regulators of dorsal forebrain development. *Development* **124**, 2203–2212 (1997).
1190 47. Burtscher, I., Barkey, W. & Lickert, H. Foxa2-venus fusion reporter mouse line allows
1191 live-cell analysis of endoderm-derived organ formation: Foxa2-Venus Fusion Reporter.
1192 *genesis* **51**, 596–604 (2013).
1193 48. Chu, V. T. *et al.* Efficient generation of Rosa26 knock-in mice using CRISPR/Cas9 in
1194 C57BL/6 zygotes. *BMC Biotechnol.* **16**, 4 (2016).
1195 49. Ran, F. A. *et al.* Genome engineering using the CRISPR-Cas9 system. *Nat. Protoc.* **8**,
1196 2281–2308 (2013).
1197 50. Matsumoto, K. *et al.* Advanced CUBIC tissue clearing for whole-organ cell profiling.
1198 *Nat. Protoc.* **14**, 3506–3537 (2019).
1199 51. Haase, R. *et al.* CLIJ: GPU-accelerated image processing for everyone. *Nat. Methods* **17**,
1200 5–6 (2020).
1201 52. Stirling, D. R. *et al.* CellProfiler 4: improvements in speed, utility and usability. *BMC*
1202 *Bioinformatics* **22**, 433 (2021).
1203 53. Berg, S. *et al.* ilastik: interactive machine learning for (bio)image analysis. *Nat. Methods*
1204 **16**, 1226–1232 (2019).
1205 54. Mitchell, N. P. & Cislo, D. J. *TubULAR: Tracking* in toto *deformations of dynamic*
1206 *tissues via constrained maps*. http://biorxiv.org/lookup/doi/10.1101/2022.04.19.488840
1207 (2022) doi:10.1101/2022.04.19.488840.
1208 55. Rodolà, E., Bulò, S. R. & Cremers, D. Robust Region Detection via Consensus
1209 Segmentation of Deformable Shapes. *Comput. Graph. Forum* **33**, 97–106 (2014).
1210 56. Crane, K., Livesu, M., Puppo, E. & Qin, Y. A Survey of Algorithms for Geodesic Paths
1211 and Distances. (2020) doi:10.48550/ARXIV.2007.10430.
1212 57. Pallares, L. F., Picard, S. & Ayroles, J. F. TM3'seq: A Tagmentation-Mediated 3'
1213 Sequencing Approach for Improving Scalability of RNAseq Experiments. *G3*
1214 *GenesGenomesGenetics* **10**, 143–150 (2020).

1215 58. Truett, G. E. *et al.* Preparation of PCR-Quality Mouse Genomic DNA with Hot Sodium
1216 Hydroxide and Tris (HotSHOT). *BioTechniques* **29**, 52–54 (2000).
1217